PHYSICAL REVIEW LETTERS **123,** 208003 (2019)

Featured in Physics

Topology, Geometry, and Mechanics of Strongly Stretched and Twisted Filaments: Solenoids, Plectonemes, and Artificial Muscle Fibers

Nicholas Charles,[1] Mattia Gazzola,[2] and L. Mahadevan[3,4,*]
[1]*Paulson School of Engineering and Applied Sciences, Harvard University, Cambridge, Massachusetts 02138, USA*
[2]*Department of Mechanical Science and Engineering and National Center for Supercomputing Applications, University of Illinois at Urbana-Champaign, Urbana, Illinois 61801, USA*
[3]*Paulson School of Engineering and Applied Sciences, Department of Physics, Department of Organismic and Evolutionary Biology, Harvard University, Cambridge, Massachusetts 02138, USA*
[4]*Kavli Institute for Nanobio Science and Technology, Harvard University, Cambridge, Massachusetts 02138, USA*

(Received 25 August 2018; revised manuscript received 11 March 2019; published 13 November 2019)

Soft elastic filaments that can be stretched, bent, and twisted exhibit a range of topologically and geometrically complex morphologies. Recently, a number of experiments have shown how to use these building blocks to create filament-based artificial muscles that use the conversion of writhe to extension or contraction, exposing the connection between topology, geometry, and mechanics. Here, we combine numerical simulations of soft elastic filaments that account for geometric nonlinearities and self-contact to map out the basic structures underlying artificial muscle fibers in a phase diagram that is a function of the extension and twist density. We then use ideas from computational topology to track the interconversion of link, twist, and writhe in these geometrically complex physical structures to explain the physical principles underlying artificial muscle fibers and provide guidelines for their design.

DOI: 10.1103/PhysRevLett.123.208003

The bending and twisting elastic response of soft filamentous objects is a consequence of the separation of scales inherent in their slender geometries. This realization is at the heart of the classical Kirchhoff-Love theory [1,2], which considers inextensible, unshearable filaments and has spawned substantial literature [3,4]. When such filaments are twisted strongly, they deform into plectonemic structures that consist of self-braided segments and which have been observed across scales, from DNA to metal wires [5,6]. The transition between the straight and plectonemic structures in inextensible filaments has been explored extensively in both a deterministic and a stochastic setting [7–10] and continues to be a topic of interest. However, filaments made of soft elastomeric materials are also easily extensible and shearable, and their study is interesting for a range of applications such as biological tissue mechanics, soft robotics, etc [11]. Among the simplest behaviors that harnesses these modes of deformation is the controlled transition between straight filaments and tightly coiled helical shapes (solenoids) originally observed in textiles [12], quantified experimentally in elastomers [13], and then rediscovered in the context of heat-driven artificial muscles [14]. These energy-harvesting devices rely on the conversion of twist and bend into extension [15–17], as solenoids untwist and stretch. Here we consider the interplay between topology, geometry, and mechanics in strongly stretched and twisted filaments and their functional consequences.

We describe a filament by a centerline position vector $\bar{x}(s,t) \in \mathbb{R}^3$ ($s \in [0, L_0]$ is the material coordinate of the rod of rest length L_0 at time t), while the orientation of its cross section is defined by an initially orthonormal triad associated with the director vectors $\bar{\boldsymbol{d}}_i(s,t), i = 1, 2, 3$, where $\bar{\boldsymbol{d}}_3(s,t)$ is normal to the material cross section of the filament. Then, the transformation of the body-fixed frame (quantities without overbar) to the lab-fixed frame (quantities with overbar) can be written in terms of the rotation matrix $\boldsymbol{Q}(s,t) = \{\bar{\boldsymbol{d}}_1, \bar{\boldsymbol{d}}_2, \bar{\boldsymbol{d}}_3\}^{-1}$ [see Fig. 1(a)].

In general, the centerline tangent $\partial_s \bar{\boldsymbol{x}} = \bar{\boldsymbol{x}}_s$ does not point along the normal to the cross section $\bar{\boldsymbol{d}}_3(s,t)$. The deviation between these vectors characterizes local extension and shear $\boldsymbol{\sigma} = \boldsymbol{Q}(\bar{\boldsymbol{x}}_s - \bar{\boldsymbol{d}}_3) = \boldsymbol{Q}\bar{\boldsymbol{x}}_s - \boldsymbol{d}_3$ [Fig. 1(a)] and is the basis of the Cosserat rod theory [3] that allows us to include all six modes of deformation at every cross section [mathematically, this is associated with the dynamics on the full Euclidean group SE(3)]. The restriction to the Kirchhoff theory corresponds to the case $\boldsymbol{\sigma} = 0$; i.e., the normal to the cross section is also the tangent to the centerline, with $\bar{\boldsymbol{x}}_s - \boldsymbol{d}_3 = 0$.

Since many soft materials are close to being incompressible (i.e., the shear modulus is much smaller than the bulk modulus), filaments made of such materials will also be incompressible. Then, if $e = |\bar{\boldsymbol{x}}_s|$ is the local elongation factor and A is the local cross-sectional area, Ae is constant locally. Accounting for this nonlinear constraint along with a simple materially linear constitutive law provides is a reasonable approximation to both neo-Hookean and Mooney-Rivlin materials (see Ref. [18] and

0031-9007/19/123(20)/208003(6)

© 2019 American Physical Society

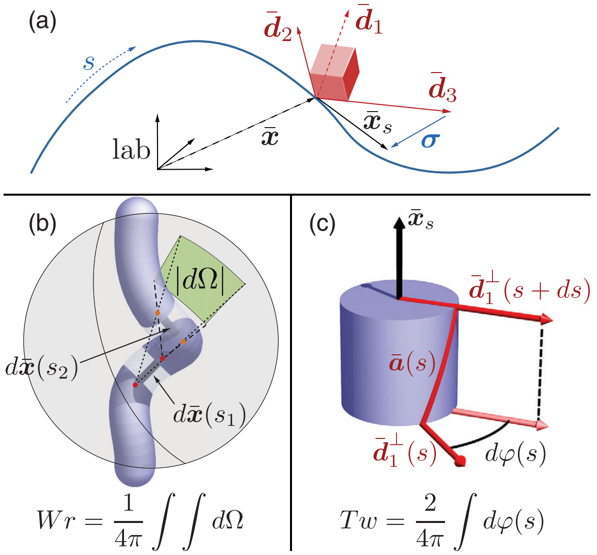
(a)
s
$\bar{\boldsymbol{d}}_2$
$\bar{\boldsymbol{d}}_1$
$\bar{\boldsymbol{d}}_3$
lab
$\bar{\boldsymbol{x}}$
$\bar{\boldsymbol{x}}_s$
$\boldsymbol{\sigma}$
(b)
$|d\Omega|$
$d\bar{\boldsymbol{x}}(s_2)$
$d\bar{\boldsymbol{x}}(s_1)$
$Wr = \frac{1}{4\pi}\int\int d\Omega$
(c)
$\bar{\boldsymbol{x}}_s$
$\bar{\boldsymbol{d}}_1^{\perp}(s+ds)$
$\bar{\boldsymbol{a}}(s)$
$\bar{\boldsymbol{d}}_1^{\perp}(s)$
$d\varphi(s)$
$Tw = \frac{2}{4\pi}\int d\varphi(s)$

FIG. 1. Geometry and topology of soft extensible filaments. (a) The filament centerline $\bar{\boldsymbol{x}}(s,t)$ and local orthogonal frame $\{\bar{\boldsymbol{d}}_1, \bar{\boldsymbol{d}}_2, \bar{\boldsymbol{d}}_3\}$. Shear and extension are defined by the vector $\boldsymbol{\sigma} = \boldsymbol{Q}\bar{\boldsymbol{x}}_s - \boldsymbol{d}_3$, while curvature and twist are defined by the vector $\mathbf{k} = \mathrm{vec}(\mathbf{Q}'\mathbf{Q}^{\mathrm{T}})$. (b) Writhe (Wr) equals the centerline's average oriented self-crossing number computed in terms of the integral of the solid angle $d\Omega$ determined by the infinitesimal centerline segments $\bar{\boldsymbol{x}}(s_1)$ and $\bar{\boldsymbol{x}}(s_2)$ (left-handed intersections are negative). (c) Twist (Tw) is the integral of the infinitesimal rotations $d\varphi$ of the auxiliary curve $\bar{\boldsymbol{a}}$ around $\bar{\boldsymbol{x}}_s$. Here, the vector $\bar{\boldsymbol{a}}$ traced out by $\bar{\boldsymbol{d}}_1^{\perp}$ (i.e., the projection of $\bar{\boldsymbol{d}}_1$ onto the normal-binormal plane) is shown in red while the curve associated with $-\bar{\boldsymbol{d}}_1$ is shown in yellow (see Fig. 2). For a closed curve Lk = Tw + Wr, where Lk (link) is the average oriented crossing number of $\bar{\boldsymbol{x}}(s)$ with $\bar{\boldsymbol{a}}(s)$.

the Supplemental Material [19] for model validation and more details about the physical model and numerical scheme, and Refs. [25–27] for alternative approaches).

Then, we may write the linear and angular momentum balance equations as [3,4,18]

$$\rho A \cdot \partial_t^2 \bar{\boldsymbol{x}} = \partial_s\left(\frac{\boldsymbol{Q}^T \boldsymbol{S}\boldsymbol{\sigma}}{e}\right) + e\bar{\boldsymbol{f}}$$

$$\frac{\rho \boldsymbol{I}}{e}\cdot \partial_t \boldsymbol{\omega} = \partial_s\left(\frac{\boldsymbol{B}\boldsymbol{k}}{e^3}\right) + \frac{\boldsymbol{k}\times\boldsymbol{B}\boldsymbol{k}}{e^3} + \left(\boldsymbol{Q}\frac{\bar{\boldsymbol{x}}_s}{e}\times\boldsymbol{S}\boldsymbol{\sigma}\right) + \left(\rho\boldsymbol{I}\cdot\frac{\boldsymbol{\omega}}{e}\right)\times\boldsymbol{\omega} + \frac{\rho\boldsymbol{I}\boldsymbol{\omega}}{e^2}\cdot\partial_t e + e\boldsymbol{c},$$

where ρ is the material density, $\bar{\boldsymbol{\omega}} = \mathrm{vec}(\partial_t \boldsymbol{Q}^T \boldsymbol{Q})$ is the local angular velocity, $\bar{\boldsymbol{k}} = \mathrm{vec}(\partial_s \boldsymbol{Q}^T \boldsymbol{Q})$ is the local strain vector (of curvatures and twist), $\boldsymbol{S}$ is the matrix of shearing and extensional rigidities, $\boldsymbol{B}$ is the matrix of bending and twisting rigidities, and $\boldsymbol{f}$, $\boldsymbol{c}$ are the body force density and external couple density (see the Supplemental Material [19] or Ref. [18] for details).

To follow the geometrically nonlinear deformations of the filament described by the equations above, we employ a recent simulation framework [18], wherein the filament is discretized in to a set of $n+1$ vertices $\{\bar{\boldsymbol{x}}_i\}_{i=0}^{n}$ connected by edges $\bar{\boldsymbol{e}}^i = \bar{\boldsymbol{x}}_{i+1} - \bar{\boldsymbol{x}}_i$, and a set of n frames $\{\boldsymbol{Q}^i\}_{i=0}^{n-1}$. The resulting discretized system of equations is integrated using an overdamped second-order scheme, reducing the dynamical simulation to a quasistatic process, while accounting for self-contact forces, internal viscous forces, and the dynamic modification of the filament geometry and stiffness (see Supplemental Material [19] and Ref. [18] for details) while ignoring friction.

To track the knotlike structures that form when the stretched and twisted filament can contact itself, we take advantage of the Calugareanu-Fuller-White theorem [28,29]: Lk = Tw + Wr. Here, link is the oriented crossing number (or Gauss linking integral) of the centerline and auxiliary curve $\bar{\boldsymbol{a}}(s)$ (Fig. 1) averaged over all projection directions [30], writhe is the link of the centerline with itself [31], and twist denotes the local rotation of the auxiliary curve about the centerline tangent. In a discrete setting, we compute writhe, link, and twist of the filament modeled as an open ribbon following Ref. [32], as illustrated in Fig. 1 (see the Supplemental Material [19] for details).

When inextensible filaments are stretched and twisted, a range of localized and self-contacting structures arise and have been well studied in both a deterministic and stochastic setting [9,10,33–36]. For highly stretched and twisted filaments, the phase space of possibilities is much richer, and in particular, a new morphological phase associated with tightly coiled helices (solenoids) appears [12,13]. To characterize these morphologies, we simulate twisting a filament clamped at one end and prestretched by a constant axial load. We first use an axial load ~25 times the critical compressive buckling force of a corresponding inextensible filament $F_C = (\pi^2 EI)/L_0^2$. In Fig. 2(a), denoting by a the filament rest configuration radius, we show that when a critical dimensionless twist density Φa is reached, the filament becomes unstable to bending, leading to the formation of a plectoneme, converting twist to writhe. As the twist is increased further, occasionally the plectoneme can partially untie itself by slipping a loop over an end point, allowing the link to escape the system (see Fig. S3 in the Supplemental Material [19]). In Fig. 2(b), we repeat the simulation but quadruple the stretching strain and see that at a critical value of Φa, the filament again becomes unstable to bending but now leads to a qualitatively different equilibrium configuration: a tightly coiled helical solenoid. We note that substantial prestretch is the crucial prerequisite for solenoid formation, while shearing is found to be unimportant (see Supplemental Material [19] for details). While both plectonemes and solenoids convert twist to writhe in steps, they are otherwise quite different. Plectonemes lead to braids made of oppositely chiral helices, while solenoids lead to a single compact helix.

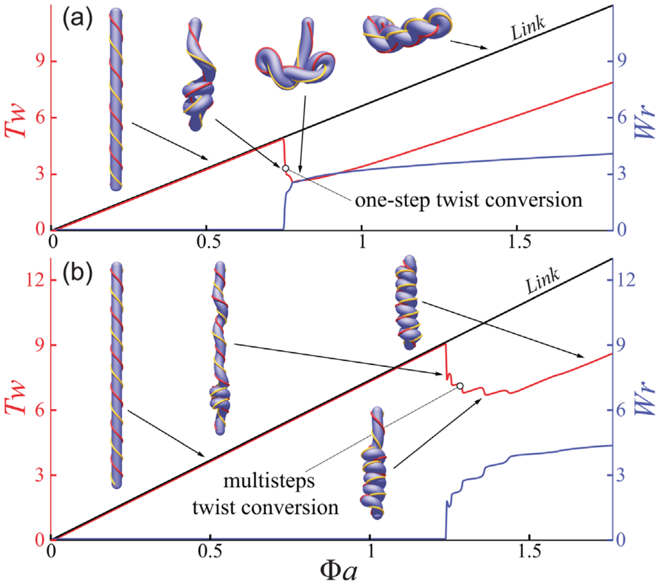

FIG. 2. Variation of the link, twist, and writhe as a function of the dimensionless twist density Φa (a is the filament radius in the rest configuration). (a) To replicate the experimental observations in Ref. [13], we use a constant vertical load $F \approx 25F_C$ to produce a plectoneme ($F_C = \pi^2 EI/L_0^2$ is the buckling force for an inextensible rod; see Video S1 in the Supplemental Material [19] and Ref. [37]). (b) We repeat the simulation with $F \approx 90F_C$, stretching the filament to deformed length $L \approx 1.16L_0$. Increased stretching leads to an overall similar conversion of twist to writhe leading to tightly packed solenoidal structures (see Video S2 and the Supplemental Material [19] for plots of filament energy). Simulation settings (see Supplemental Material [19]): length $L_0 = 1$ m, $a = 0.025L_0$, Young's modulus $E = 1$ MPa, shear modulus $G = 2E/3$, $\boldsymbol{S} = \text{diag}(4GA/3, 4GA/3, EA)$ N, $\boldsymbol{B} = \text{diag}(EI_1, EI_2, GI_3)$ N m^2.

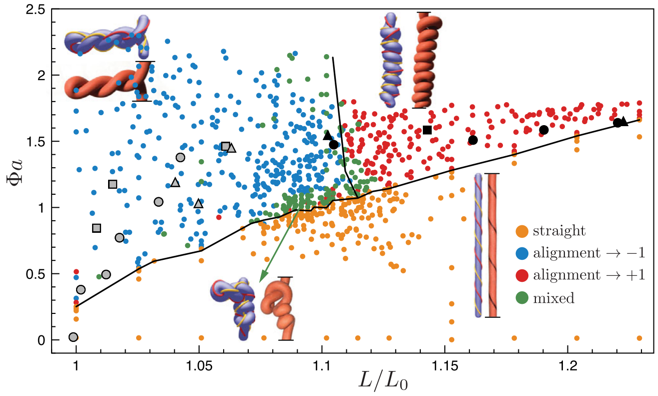

FIG. 3. Morphological phase space. We simulate a filament prestretched to L/L_0 by a constant axial load and twisted by an angle Φa, as in Fig. 2. By computing centerline relative alignment in neighboring loops, we find four phases: straight, plectoneme, solenoid, and plectoneme-solenoid combinations. Plectoneme alignment ≈ -1, solenoid alignment ≈ 1, and transition configuration alignments approach 0 (dark green). For $L/L_0 \gtrsim 1.1$, solenoids are preferred. We expect Φ_{critical} to scale linearly with L/L_0 at high extension, in agreement with this plot. Our results agree qualitatively with experiments [13] (shown in black dots; see Supplemental Material [19] for details). Hollow symbols denote plectoneme transitions, while solid points denote solenoid transitions; different shapes correspond to different filament parameters (Supplemental Material [19]). Simulation settings (Supplemental Material [19]): $L_0 = 1$ m, $a = 0.025L_0$, $E = 1$ MPa, $G = 2E/3$, $\boldsymbol{S} = \text{diag}(4GA/3, 4GA/3, EA)$ N, $\boldsymbol{B} = \text{diag}(EI_1, EI_2, GI_3)$ N m^2.

Furthermore, a plectoneme loop converts much more twist to writhe than a solenoid does as it coils up (Fig. 2). However, the tightly coiled nature of the solenoidal coil makes it more stable under stretching.

We now turn to explain the experimental observations and morphological phase diagram that span the twist density-extensional strain $(\Phi a) - (L/L_0)$ phase space [13] (L is the stretched filament length). Using randomly sampled twist densities and extensions in this phase space, we classify each resulting configuration on the spectrum from plectoneme to solenoid using the average relative alignment of tangent vectors at filament segments which are adjoining in absolute coordinates but separated in material coordinates, i.e., $\text{avg}_{i=1}^{n}[\text{sgn}(\bar{\boldsymbol{e}}^i \cdot \bar{\boldsymbol{e}}^k)]$, where $k = \text{argmin}(|\bar{\boldsymbol{x}}_k - \bar{\boldsymbol{x}}_i|)$ subject to $|k - i| > (5na/L_0)$ and $|\bar{\boldsymbol{x}}_k - \bar{\boldsymbol{x}}_i|(2 + \epsilon)a$, with $\epsilon = 0.2$ (empirically determined to maximize classification accuracy). Plectoneme loops involve two strands entwined in antiparallel directions (alignment → −1), while segments of adjacent solenoid loops tend to lie parallel (alignment → 1), and straight segments do not contribute to the average. In Fig. 3 we show four qualitatively different filament configurations: rectilinear, plectoneme, solenoid, and a mixed state with features of both plectonemes and solenoids. Indeed, the distinction between solenoid and plectoneme becomes blurred near the triple point. These simulations agree qualitatively with experimental observations [13], as illustrated in Fig. 3; the small quantitative discrepancy between experiments and simulations is likely due to our neglect of friction. It is worth pointing out that the region of solenoid-plectoneme coexistence can be expanded by having an active agent (for example, a DNA-binding enzyme) capable of either relaxing the internal axial tension and/or inducing excess twist in the filament locally. This allows for the formation of a plectoneme in the compressed segment, after which, upon further twisting, a solenoid forms below the lifted point (Supplemental Material [19] and Fig. S9), with similarities to loop formation in chromosomes [38–40].

Our results also explain earlier observations [12] that describe straight-plectoneme-solenoid transitions in terms of varying twist density and correspond to tracing horizontal and diagonal paths through the present extension-twist density phase diagram (see Supplemental Material [19]). Indeed, horizontally exiting the solenoid region in Fig. 3 to the right, by gradually displacing the lower solenoid end point away from the top leads to a steplike

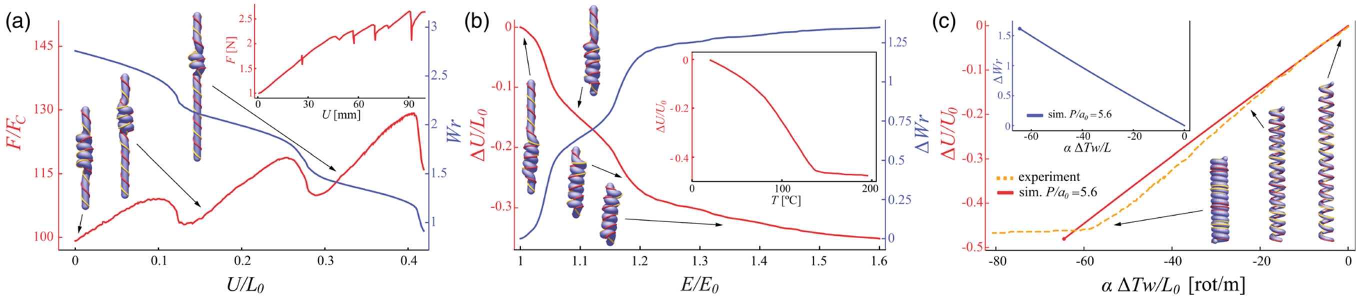

FIG. 4. Actuation of fiber-based artificial muscles that use the straight-solenoid transition. (a) Passive extension via solenoid loss. We displace the unclamped end $\bar{\boldsymbol{x}}_n$ of a solenoid formed as in Fig. 3 with a load $\approx 99F_C$ a distance ΔU in the direction $\bar{\boldsymbol{x}}_n - \bar{\boldsymbol{x}}_0$ and plot force on $\bar{\boldsymbol{x}}_n$ qualitatively reproducing experiments [13] (inset; see Video S13 in the Supplemental Material [19]). Simulation settings (Supplemental Material): $L_0 = 1$ m, $a = 0.025L_0$, $E = 1$ MPa, $G = 2E/3$, $\boldsymbol{S} = \mathrm{diag}(4GA/3, 4GA/3, EA)$ N, $\boldsymbol{B} = \mathrm{diag}(EI_1, EI_2, GI_3)$ N m^2. (b) Active work done by changing the temperature, which effectively increases filament rigidity, here simply modeled by increasing the Young's modulus E of the material. This leads to the formation of a solenoidal loop in a stretched twisted filament as in Fig. 3 with a load $\approx 116\ F_C$ as E_0 increases gradually from 1 MPa, showing displacement ΔU of $\bar{\boldsymbol{x}}_n$ and increase in writhe $\Delta\mathrm{Wr}$ from initial coil writhe, reproducing experiments [14] (inset; see Video S3 in the Supplemental Material [19]). (c) Contraction of twisted and coiled nylon polymer muscle formed by inserting twist and annealing into a helix. Filament radius doubles from initial radius $a_0 = 0.01$ m, while twist decreases to keep ak_3 constant. Numerical slope and onset of self-contact (shown as a point) agree closely with experimental results [14] (see Supplemental Material [19] for details). Beyond self-contact, radial growth pushes adjacent loops farther apart leading to helix elongation. Note that $\Delta\mathrm{Tw} + \Delta\mathrm{Wr} < 0$ in the inset. Indeed, link escapes from the free boundary due to revolution of the free filament end point around the helix axis, reducing the number of loops in the helix (see Supplemental Material [19] Fig. S7 and Videos S4 and S5). Simulation settings (Supplemental Material [19]): $L_0 = 1$ m, $a = 0.025L_0$, $E = 30$ GPa, $G = 2E/3$, $\boldsymbol{S} = \mathrm{diag}(4GA/3, 4GA/3, EA)$ N, $\boldsymbol{B} = \mathrm{diag}(EI_1, EI_2, GI_3)$ N m^2. Note that pitch P, $\alpha = 100$, number of loops, and helix radius determine L_0.

solenoid *loss* process. We track the required force and resulting change in writhe [Fig. 4(a)]. The solenoid remains mostly coiled, resisting stretching with a linear-force-displacement relation, until a critical displacement at which it uncoils by one pitch and the process starts again. This stepwise uncoiling stems from a kinematic competition similar to solenoid formation: stretching the filament increases the energy required to maintain a constant number of coils. The simulated sawtooth-force-displacement pattern agrees qualitatively with experiments [13].

Finally, we use our results to quantitatively explain a series of recent experiments on twisted-fiber-based artificial muscles [14,41–43] that exploit the connection between twist, writhe, and link. The fundamental mechanism in each of these studies is associated with the formation of solenoids that this leads to an increase in writhe, causing the filament to shorten and do work against external loads. In the twisted-fiber-based artificial muscles, the externally induced twist is replaced by the use of a scalar field, temperature, that drives variations in the radius and stiffness of a pretwisted filament and causes it to untwist, producing an increase in writhe.

In Fig. 4(b), we simulate this in a minimal setting by showing the effects of (temperature-induced) increase in the elastic modulus of a prestretched, twisted, and loaded filament. To increase writhe, the solenoidal state progressively invades the straight state, lifting its lower end point toward the clamped end, qualitatively reproducing experimental observations of the linear actuator [14]. The sheath-run artificial muscles [41] work similarly by relying on the conversion of untwist to writhe, while the strain-programmable artificial muscles [42] generate a tensile stroke via temperature-induced differential expansion in a bilayer that is tantamount to changing the natural curvature of a filament dynamically. Finally, the torsional actuator [43] generates torque by inserting twist into a filament and then quickly lowering the filament's intrinsic twist until it vanishes. Rather than replicate all the different variants of the fiber-based artificial muscles, here we limit ourselves to just two simple cases: the linear actuator [14] and the rotary or torsional actuator [43].

To capture the mechanics of the linear actuator, we initialize a filament with intrinsic twist and numerically anneal the filament into a uniform coil with space between adjacent loops, replicating the plastic deformation process by which twisted and coiled polymer muscles are formed. The fibers used in Ref. [14] expand radially and contract axially when heated; however, as noted quantitatively in Ref. [44], considering radial growth with fixed fiber length is sufficient. While our model applies to an isotropic filament, we can simulate anisotropic expansion-driven untwist by following the mechanical analogy in Ref. [14]. Imagine winding an inextensible string around a fiber, attaching it on both fiber ends. To keep the length of the string constant, the fiber would have to untwist to expand. Mathematically, this requires ak_3 to stay constant. Hence, we prescribe a radial growth rate and continuously update the intrinsic twist $\hat{k}_3$ to keep $a\hat{k}_3$ constant [45]. For a homochiral coil, the resulting untwist leads to contraction (Fig. 4), but in a heterochiral coil, untwisting leads to elongation (Supplemental Material [19] Fig. S8 and Videos S6 and S7). In Fig. 4(c), we show the change in Wr and contraction for a simulated coil with initial nonzero twist density. The coils contract at the same scaled rate as experiments until adjacent loops come into contact (see Supplemental Material [19] for details of varying P/a_0). To capture the mechanics of the rotary actuator [43], we initialize the filament with intrinsic twist which is then rapidly decreased to mimic the effect of annealing via heating leading to rotary motion (see Supplemental Material [19] Sec. S7, Video S14).

Altogether, our study links topology, geometry, and mechanics to explain the complex morphology of soft, strongly stretched, twisted filaments, Additionally, we showed how twist, link and writhe can be interconverted via either external loads or temperature variations, thus allowing us to quantify recent experiments on artificial muscle fibers, setting the stage for the study of complex braided, knotted, and twisted filament configurations in a range of new settings.

We thank Andrew McCormick for his preliminary contributions to the project, and the UIUC Blue Waters project (Grants No. OCI-0725070 and No. ACI-1238993) (M. G.), the National Science Foundation Emerging Frontiers in Research and Innovation: Continuum, Compliant, and Configurable Soft Robotics Engineering (NSF EFRI C3 SoRo) Grant No. 1830881 (M. G.), and the NSF CAREER Grant No. 1846752 (M. G.), the Harvard Materials Research Science and Engineering Center National Science Foundation Division of Materials Research (MRSEC NSF DMR) Grant No. 14-20570 (L. M.), and Harvard Designing Materials to Revolutionize and Engineering our Future (DMREF): Biologically Inspired Optimized Materials and Technologies Transformed by Evolutionary Rules (BioMatter) National Science Foundation Division of Materials Research (NSF DMR) Grant No. 1533985 (L. M.) for partial financial support.

---

[*] lmahadev@g.harvard.edu

[1] G. Kirchhoff, J. Reine. Angew. Math. **56**, 285 (1859).

[2] A. E. H. Love, *A Treatise on the Mathematical Theory of Elasticity* (Cambridge University Press, Cambridge, England, 1892).

[3] S. S. Antman, *Nonlinear Problems of Elasticity* (Springer, New York, 2004).

[4] O. M. O'Reilly, *Modeling Nonlinear Problems in the Mechanics of Strings and Rods: The Role of the Balance Laws* (Springer, New York, 2017).

[5] D. Beard and T. Schlick, J. Chem. Phys. **112**, 7323 (2000).

[6] J. Coyne, IEEE Journal of Oceanic Engineering **15**, 72 (1990).

[7] G. H. M. Van der Heijden and J. M. T. Thompson, Nonlinear Dyn. **21**, 71 (2000).

[8] D. M. Stump, W. B. Fraser, and K. E. Gates, Proc. R. Soc. A **454**, 2123 (1998).

[9] W. K. Olson and P. S. Zhang, Methods Enzymol. **203**, 403 (1991).

[10] J. F. Marko and S. Neukirch, Phys. Rev. E **85**, 011908 (2012).

[11] X. Zhang, F. Chan, T. Parthasarathy, and M. Gazzola, Nat. Commun. **10**, 4825 (2019).

[12] J. W. S. Hearle and A. E. Yegin, J. Text. Inst. **63**, 490 (1972).

[13] A. Ghatak and L. Mahadevan, Phys. Rev. Lett. **95**, 057801 (2005).

[14] C. Haines, N. Li, G. Spinks, A. Aliev, J. Di, and R. Baughman, Proc. Natl. Acad. Sci. U.S.A. **113**, 11709 (2016).

[15] S. H. Kim, C. Haines, N. Li, K. J. Kim, T. J. Mun, C. Choi, J. Di, Y. J. Oh, J. P. Oviedo, J. Bykova *et al.*, Science **357**, 773 (2017).

[16] S. H. Kim, H. J. Sim, J. S. Hyeon, D. Suh, G. M. Spinks, R. Baughman, and S. J. Kim, Sci. Rep. **8**, 8712 (2018).

[17] N. Atikah, L. Y. Weng, A. Anuar, C. C. Fat, I. Z. Abidin, and K. S. M. Sahari, AIP Conf. Proc. **1883**, 020042 (2017).

[18] M. Gazzola, L. Dudte, A. McCormick, and L. Mahadevan, R. Soc. Open Sci. **5**, 171628 (2018).

[19] See Supplemental Material at http://link.aps.org/supplemental/10.1103/PhysRevLett.123.208003 for further discussion of model validity and for more details about the physical model, numerical scheme and representative simulations, which includes Refs. [20–24].

[20] L. R. G. Treloar, Trans. Faraday Soc. **40**, 59 (1944).

[21] S. Reese and P. Wriggers, Comput. Methods Appl. Mech. Eng. **148**, 279 (1997).

[22] O. Ahumada, M. Cocca, G. Gentile, E. Martuscelli, and L. D'Orazio, Textile research Journal : publication of Textile Research Institute, Inc and the Textile Foundation **74**, 1001 (2004).

[23] D. Clark, W. Fleming, R. Bosanquet, and E. Down, Phys. Med. Biol. **41**, 1233 (1996).

[24] O. Rodrigues, Journal de Mathématique Pures et Appliquées **5**, 380 (1840).

[25] J. Spillmann and M. Teschner, *Symposium on Computer Animation: Proceedings of the 2007 ACM SIGGRAPH/Eurographics Symposium on Computer Animation* (2007).

[26] B. Audoly, N. Clauvelin, P. T. Brun, M. Bergou, E. Grinspun, and M. Wardetzky, J. Comput. Phys. **253**, 18 (2013).

[27] M. Bergou, M. Wardetzky, S. Robinson, B. Audoly, and E. Grinspun, ACM Trans. Graph. **27**, 1 (2008).

[28] F. B. Fuller, Proc. Natl. Acad. Sci. U.S.A. **75**, 3557 (1978).

[29] G. Calugareanu, Rev. Math. Pures Appl **4**, 5 (1959).

[30] R. Ricca and B. Nipoti, J. Knot Theory Ramif. **20**, 1325 (2011).

[31] F. B. Fuller, Proc. Natl. Acad. Sci. U.S.A. **68**, 815 (1971).

[32] K. Klenin and J. Langowski, Biopolymers **54**, 307 (2000).

[33] S. Gerbode, J. Puzey, A. McCormick, and L. Mahadevan, Science **337**, 1087 (2012).

[34] A. R. Champneys, G. H. M. Van der Heijden, and J. M. T. Thompson, SIAM J. Appl. Math. **59**, 198 (1998).

[35] A. Goriely and M. Tabor, Phys. Rev. Lett. **80**, 1564 (1998).

[36] J. D. Moroz and P. Nelson, Proc. Natl. Acad. Sci. U.S.A. **94**, 14418 (1997).

[37] A. Majumdar and A. Raisch, Nonlinearity **27**, 2841 (2014).

[38] G. Fudenberg, M. Imakaev, C. Lu, A. Goloborodko, N. Abdennur, and L. Mirny, Cell Rep. **15**, 2038 (2016).

[39] M. Ganji, I. A. Shaltiel, S. Bisht, E. Kim, A. Kalichava, C. H. Haering, and C. Dekker, Science **360**, 102 (2018).

[40] B. Soh, V. Narsimhan, A. R. Klotz, and P. S. Doyle, Soft Matter **14**, 1689 (2018).

[41] J. Mu *et al.*, Science **365**, 150 (2019).

[42] M. Kanik *et al.*, Science **365**, 145 (2019).

[43] J. Yuan, W. Neri, C. Zakri, P. Merzeau, K. Kratz, A. Lendlein, and P. Poulin, Science **365**, 155 (2019).

[44] C. Lamuta, S. Messelot, and S. Tawfick, Smart Mater. Struct. **27**, 055018 (2018).

[45] Note that we update *intrinsic* twist (twist of the filament in its rest configuration) $\widehat{k}_3$ rather than true twist k_3, since k_3 must evolve according to the equations of motion. The filament twisting strain is defined by $k_3 - \widehat{k}_3$, so the filament deforms to try to make $k_3 = \widehat{k}_3$. After the onset of self-contact, radial growth pushes adjacent loops apart, lowering filament writhe and thereby forcing the filament to retwist despite an ever-increasing intrinsic twist.

Supporting Information for "Topology, geometry and mechanics of strongly stretched and twisted filaments" by N. Charles, M. Gazzola and L. Mahadevan

S1. SIMULATION METHOD

A. Mathematical Model

We model our filament using the Cosserat rod theory [1] and follow a similar notation to [2] and [3]. In this context, we describe the filament by a centerline $\bar{\boldsymbol{x}}(s,t) \in \mathbb{R}^3$ and rotation matrix $\boldsymbol{Q}(s,t) \in SO(3)$ which relates the local $\boldsymbol{d}_i$ and global frames $\bar{\boldsymbol{d}}_i$ via $\boldsymbol{d}_i = \boldsymbol{Q}\bar{\boldsymbol{d}}_i$ where $\boldsymbol{Q}(s,t) = \{\bar{\boldsymbol{d}}_1, \bar{\boldsymbol{d}}_2, \bar{\boldsymbol{d}}_3\}^{-1}$. We define $s \in [0, L_0]$ as the material coordinate of our (unstretched) length L_0 rod and t as time. We denote the stretched filament length by L. Vectors expressed in the global frame are denoted by bars.

If the rod is unsheared, $\bar{\boldsymbol{d}}_3$ points along the centerline tangent $\bar{\boldsymbol{x}}_s$ while $\bar{\boldsymbol{d}}_1$ and $\bar{\boldsymbol{d}}_2$ span the normal-binormal plane. Shearing and extension shift $\bar{\boldsymbol{d}}_3$ away from $\bar{\boldsymbol{x}}_s$, which we quantify with the shear vector $\boldsymbol{\sigma} = \boldsymbol{Q}(\bar{\boldsymbol{x}}_s - \bar{\boldsymbol{d}}_3) = \boldsymbol{Q}\bar{\boldsymbol{x}}_s - \boldsymbol{d}_3$ in the *local* frame.

The curvature (and twist) vector $\bar{\boldsymbol{k}} = \mathrm{vec}(\partial_s \boldsymbol{Q}^T \boldsymbol{Q})$ encodes $\boldsymbol{Q}$'s rotation rate along the material coordinate $\partial_s \bar{\boldsymbol{d}}_i = \bar{\boldsymbol{k}} \times \bar{\boldsymbol{d}}_i$, while the temporal rate of change of the rotation matrix characterizes the angular velocity vector $\bar{\boldsymbol{\omega}} = \mathrm{vec}(\partial_t \boldsymbol{Q}^T \boldsymbol{Q})$ and allows us to write $\partial_t \bar{\boldsymbol{d}}_j = \bar{\boldsymbol{\omega}} \times \bar{\boldsymbol{d}}_j$, where $\mathrm{vec}(\boldsymbol{M})$ denotes the vector corresponding to a skew-symmetric matrix $\boldsymbol{M}$. Note that the following identities hold for rotation matrices:

$$\boldsymbol{Q}\left(\partial_t \bar{\boldsymbol{x}}\right) = \partial_t \boldsymbol{x} + \boldsymbol{\omega} \times \boldsymbol{x} \qquad \boldsymbol{Q}\left(\partial_s \bar{\boldsymbol{x}}\right) = \partial_s \boldsymbol{x} + \boldsymbol{k} \times \boldsymbol{x}$$

We also define the velocity of the centerline $\bar{\boldsymbol{v}} = \partial_t \bar{\boldsymbol{x}}$ and, in the rest configuration, the bending stiffness matrix $\boldsymbol{B}$, shearing stiffness matrix $\boldsymbol{S}$, inertia matrix $\boldsymbol{I}$, cross-sectional area A, and mass per unit length ρ.

Having characterized the kinematics of the geometry and motion of the filament, we turn to characterizing the dynamics of the filament. We assume that the filament is circular with a second area moment of inertia $\boldsymbol{I}$, cross-sectional area A and mass per unit length ρ.

We assume the material of the soft filament is incompressible, so that Ae is constant, where $e = |\bar{\boldsymbol{x}}_s|$ is the elongation factor. This allows us to use a simple materially linear constitutive law that is a good compromise between neo-Hookean and Mooney-Rivlin (see section S1 C for validation, and a discussion of the role of irreversible deformations in the context of experiments).

In particular, the (cross-sectionally integrated) stress resultant $\boldsymbol{F}$ and moment resultant $\boldsymbol{M}$ are proportional to the curvature and shear vectors, i.e. $\boldsymbol{F} = (\boldsymbol{S}/e)\boldsymbol{\sigma}, \boldsymbol{M} = (\boldsymbol{B}/e^2)(\boldsymbol{k}/e)$ where the shearing (and stretching) stiffness matrix $\boldsymbol{S}$ and bending (and twisting) stiffness matrix $\boldsymbol{B}$ are scaled by the filament's local extension, and $\boldsymbol{k}$ is scaled by e to obtain curvature with respect to deformed arclength.

Referring to [2], we obtain the equations:

$$\partial_t \bar{\boldsymbol{x}} = \bar{\boldsymbol{v}} \tag{S1}$$

$$\partial_t \bar{\boldsymbol{d}}_j = \left(\boldsymbol{Q}^T \boldsymbol{\omega}\right) \times \bar{\boldsymbol{d}}_j \tag{S2}$$

$$\rho A \cdot \partial_t^2 \bar{\boldsymbol{x}} = \partial_s \left(\frac{\boldsymbol{Q}^T \boldsymbol{S}\boldsymbol{\sigma}}{e}\right) + e\bar{\boldsymbol{f}} - \nu_t \boldsymbol{v} \tag{S3}$$

$$\frac{\rho \boldsymbol{I}}{e} \cdot \partial_t \boldsymbol{\omega} = \partial_s \left(\frac{\boldsymbol{B}\boldsymbol{k}}{e^3}\right) + \frac{\boldsymbol{k} \times \boldsymbol{B}\boldsymbol{k}}{e^3} + \left(\boldsymbol{Q}\frac{\bar{\boldsymbol{x}}_s}{e} \times \boldsymbol{S}\boldsymbol{\sigma}\right) + \left(\rho \boldsymbol{I} \cdot \frac{\boldsymbol{\omega}}{e}\right) \times \boldsymbol{\omega} + \frac{\rho \boldsymbol{I}\boldsymbol{\omega}}{e^2} \cdot \partial_t e + e\boldsymbol{c} - \nu_r \boldsymbol{\omega} \tag{S4}$$

where $e = |\bar{\boldsymbol{x}}_s|$, $\boldsymbol{f}$ is the external force line density, $\boldsymbol{c}$ is the external couple line density, ρA is the mass line density, $\rho \boldsymbol{I}$ is the mass second moment of inertia per unit length, and $j \in \{1, 2, 3\}$. We have also explicitly included external damping terms $-\nu_t \boldsymbol{v}$ and $-\nu_r \boldsymbol{\omega}$, following [2]. For all simulations in this letter, we set $\nu_t = \nu_r \equiv \gamma$ and vary γ between simulations. We modify the equations of [2] by adding internal damping (see section S3).

Consistent with our stress-strain relations, we take energies to be quadratic in displacements from the filament rest configuration, again noting that stiffness depend on local strain. Referring to [2], the shear and stretch (E_S), bending and twist (E_B), translational (E_T) and rotational (E_R) energies are:

$$E_S = \frac{1}{2} \int_0^{L_0} \frac{\boldsymbol{\sigma}^T \boldsymbol{S}\boldsymbol{\sigma}}{e} ds \tag{S5}$$

$$\begin{aligned}
E_B =& \frac{1}{2}\int_0^{L_0} \frac{\boldsymbol{k}^T \boldsymbol{B}\boldsymbol{k}}{e^3} ds && \text{(S6)}\\
E_T =& \frac{1}{2}\int_0^{L_0} \rho A \bar{\boldsymbol{v}}^T \cdot \bar{\boldsymbol{v}} ds && \text{(S7)}\\
E_R =& \frac{1}{2}\int_0^{L_0} \frac{\rho \boldsymbol{\omega}^T \boldsymbol{I}\boldsymbol{\omega}}{e} ds && \text{(S8)}
\end{aligned}$$

To separate E_S into the components coming from shear and stretch (which is required to generate Fig. S1, S8b, S7b and S6b), we note that σ_3 encodes stretch, while σ_1 and σ_2 capture shear along $\boldsymbol{d}_1$ and $\boldsymbol{d}_2$, respectively. Thus for diagonal shear/stretch matrices $E_{stretch} = \frac{1}{2}\int_0^{L_0} \frac{(\sigma_3)^2 S_{33}}{e} ds$ where S_{33} is the $(\boldsymbol{d}_3, \boldsymbol{d}_3)$ component of $\boldsymbol{S}$. $E_S - E_{stretch} = E_{shear}$. Similarly, for diagonal bending/twist matrices $E_{twist} = \frac{1}{2}\int_0^{L_0} \frac{(k_3)^2 B_{33}}{e^3} ds$ and $E_{bending} = E_B - E_{twist}$. In Fig. S1 and S2 we show evolution of energy over twist density corresponding to the geometric changes shown in Fig. 2 and 4b of the main text.

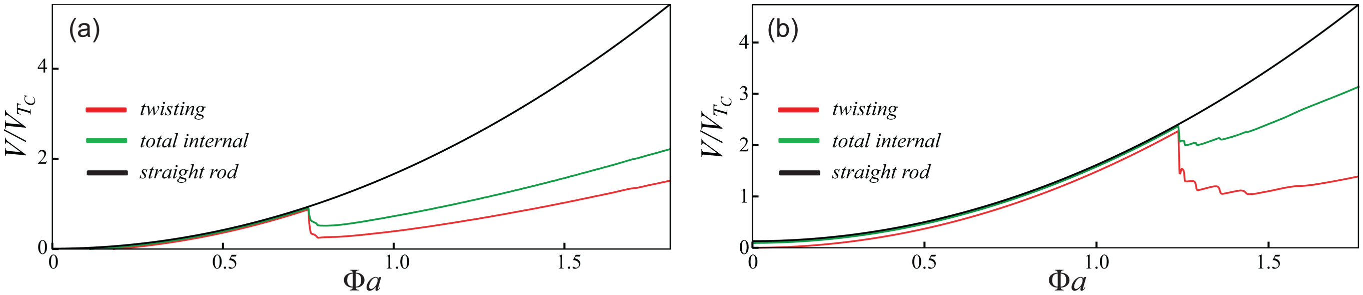

FIG. S1: Twisting and total internal energy of a filament and total internal energy of an equivalently twisted and stretched straight filament over dimensionless twist density Φa of an equivalently twisted and stretched straight filament. **(a)** corresponds to Fig. 2a and **(b)** to Fig. 2b. Energies (V) are plotted relative to $V_{T_C} = B_{33}(2\pi R_{\text{crit}})^2/2$, the maximal twisting energy before deformation of an equivalent straight *inextensible* rod under a tensile force $F = 125$ N $\approx 41 F_C$. Here $R^2_{\text{crit}} = B_{11}(B_{11}\pi^2 + F L_0^2)/(B_{33}^2\pi^2)$, B_{33} is twisting stiffness, and B_{11} is bending stiffness [4, 5]. Jumps in internal and twisting energy correspond to the formation of loops. Notice in **(b)** that stretching energy contributes nontrivially to the total filament energy, reaffirming that increased stretching leads to a qualitatively different energy balancing scenario than plectoneme formation. See Movies S1, S2.

B. Numerical Method

To implement the physical model numerically, we follow the spatial and temporal discretization schemes of [2] and [3]. We describe the filament centerline via $n+1$ vertices $\{\bar{\boldsymbol{x}}_i\}_{i=0}^{n}$ connected by n edges $\{\bar{\boldsymbol{e}}^i\}_{i=0}^{n-1}$ where $\bar{\boldsymbol{e}}^i = \bar{\boldsymbol{x}}_{i+1} - \bar{\boldsymbol{x}}_i$. The matrices $\{\boldsymbol{Q}^i\}_{i=0}^{n-1}$ describe the local frames associated with the edges. Translational velocities $\bar{\boldsymbol{v}}_{\boldsymbol{i}}$ and rotational velocities $\boldsymbol{\omega}^i$ give the time derivatives of $\bar{\boldsymbol{x}}_i$ and $\boldsymbol{Q}^i$ respectively. Pointwise concentrated masses at each vertex are denoted by m_i, and $\boldsymbol{F}_i$ give external forces on each vertex. Quantities associated with the vertices are described by lower indices, and quantities associated with the edges by upper indices.

Discrete curvatures are defined as the rotation needed to move from one frame to the next: $e^{\boldsymbol{k}_i d_i}\boldsymbol{Q}^i = \boldsymbol{Q}^{i+1}$, or equivalently $\boldsymbol{k}_i = \frac{\log\left(\boldsymbol{Q}^{i+1}\boldsymbol{Q}^{i^T}\right)}{d_i}$, where $d_i = \frac{1}{2}(l^i + l^{i+1})$ is the Voronoi domain associated with a vertex, and $l^i = |\bar{\boldsymbol{e}}^i|$. Discrete shears are $\boldsymbol{\sigma}^i = \boldsymbol{Q}^i \bar{\boldsymbol{x}}^i_s - \boldsymbol{d}^i_3$, where $\bar{\boldsymbol{x}}^i_s = \bar{\boldsymbol{e}}^i / |\bar{\boldsymbol{e}}^i_0|$ and $\bar{\boldsymbol{e}}^i_0$ is $\bar{\boldsymbol{e}}^i$ evaluated when the filament is at rest. The matrix exponential and logarithm can be computed with the Rodriguez rotation formulas [2, 6]. In summary, quantities associated with each vertex are: $\bar{\boldsymbol{x}}_i$, $\bar{\boldsymbol{v}}_i$, m_i and $\bar{\boldsymbol{F}}_i$. Quantities associated with material frames (hence edges) are: $\boldsymbol{Q}^i$, $\bar{\boldsymbol{e}}^i$, l^i, $\bar{\boldsymbol{x}}^i_s$, $e^i = |\bar{\boldsymbol{x}}^i_s|$, $\boldsymbol{\sigma}^i$, $\boldsymbol{\omega}^i$, A^i, $\boldsymbol{J}^i$, $\boldsymbol{B}^i$, $\boldsymbol{S}^i$, $\boldsymbol{C}^i$, where area cross-section, inertial moments, and stiffness matrices are defined as in the continuum model, and $\boldsymbol{C}^i$ is the external couple. Quantities associated with internal vertices $(\{\bar{\boldsymbol{x}}\}_{i=1}^{n-1} = \{\bar{\boldsymbol{x}}^{(int)}\}_{i=0}^{n-2})$ are: d_i, $\mathcal{E}_i$, $\boldsymbol{k}_i$, $\boldsymbol{\mathcal{B}}_i$, where $\mathcal{E}_i$ is the Voronoi domain dilatation factor and $\boldsymbol{\mathcal{B}}_i$ is the Voronoi domain bending/twist stiffness matrix (see [2]). These quantities allow the governing equations to be discretized:

$$\partial_t \bar{\boldsymbol{x}}_i = \bar{\boldsymbol{v}}_i \qquad \text{(S9)}$$

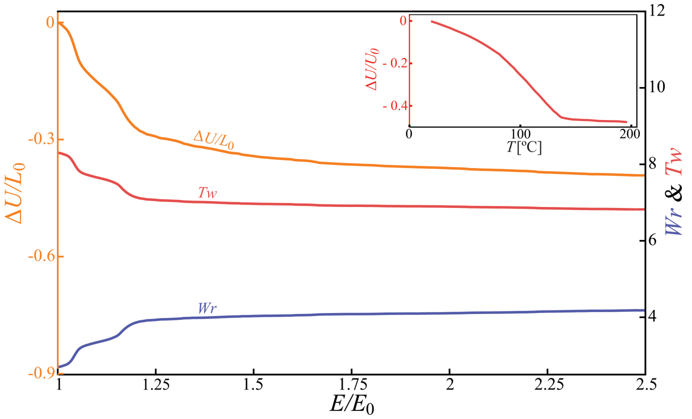

FIG. S2: Active actuation of solenoidal artificial muscle. We reproduce Fig. 4b from the main text, now showing writhe, twist, and displacement of the bottom filament endpoint toward the top as we gradually increase Young's modulus (over a larger domain than that shown in Fig. 4b). Changes in writhe and twist are equal and opposite in accordance with the CFW theorem. As the solenoid approaches the maximum coil density allowed without self-intersection, it ceases to form new loops and increases writhe by tightening existing loops. As the solenoid continues approaching maximum coil density, tightening existing loops becomes more difficult, leading to slowed contraction in agreement with experiment [7] (see inset). We naively overlay our simulated data for comparison. The bumps in our simulated data come from new loops forming. This phenomenon is not seen in [7] since the coil is annealed before stiffening in [7]. See Movie S3.

$$\partial_t \bar{\boldsymbol{d}}_j^k = \left(\boldsymbol{Q}^{k^T} \boldsymbol{\omega}^k\right) \times \bar{\boldsymbol{d}}_j^k \tag{S10}$$

$$m_i \cdot \partial_t \bar{\boldsymbol{v}}_i = \Delta^h \left(\frac{\boldsymbol{Q}^{i^T} \boldsymbol{S}^i \boldsymbol{\sigma}^i}{e^i}\right) + \bar{\boldsymbol{F}}_i - \gamma \bar{\boldsymbol{v}}_i \tag{S11}$$

$$\frac{\boldsymbol{J}}{e^k} \cdot \partial_t \boldsymbol{\omega}^k = \Delta^h \left(\frac{\boldsymbol{\mathcal{B}}_k \boldsymbol{k}_k}{\mathcal{E}_k^3}\right) + \mathcal{A}^h \left(\frac{\boldsymbol{k}_k \times \boldsymbol{B}_k \boldsymbol{k}_k}{\mathcal{E}_k^3} d_i\right) + \left(\boldsymbol{Q}^k \frac{\bar{\boldsymbol{x}}_s^k}{e^k} \times \boldsymbol{S}^k \boldsymbol{\sigma}^k\right) l^k + \left(\boldsymbol{J}^k \cdot \frac{\boldsymbol{\omega}^k}{e^k}\right) \times \boldsymbol{\omega}^k + \frac{\boldsymbol{J}^k \boldsymbol{\omega}^k}{(e^k)^2} \cdot \partial_t e^k + \boldsymbol{C}^k - \gamma \boldsymbol{\omega}^k \tag{S12}$$

where $i \in \{0, ..., n\}$, $k \in \{0, ..., n-1\}$, and $j \in \{1, 2, 3\}$. We define the discrete operators Δ^h and $\mathcal{A}^h$ by:

$$Y_{i=0,\dots,n} = \Delta^h(X_{k=0,\dots,n-1}) = \begin{cases} X_0, & i = 0 \\ X_i - X_{i-1}, & 0 < i \leq n-1 \\ -X_{n-1}, & i = n \end{cases}$$

$$Y_{i=0,\dots,n} = \mathcal{A}^h(X_{k=0,\dots,n-1}) = \begin{cases} \frac{X_0}{2}, & i = 0 \\ \frac{X_i + X_{i-1}}{2}, & 0 < i \leq n-1 \\ \frac{X_{n-1}}{2}, & i = n \end{cases}$$

We then integrate the system forward in time using a second order position Verlet time integration scheme. Explicitly, the algorithm is

$$\bar{\boldsymbol{x}}_j\left(t + \frac{\delta t}{2}\right) = \bar{\boldsymbol{x}}_j(t) + \frac{\delta t}{2} \bar{\boldsymbol{v}}_j \tag{S13}$$

$$\boldsymbol{Q}^i\left(t + \frac{\delta t}{2}\right) = \exp\left(\frac{\delta t}{2} \boldsymbol{\omega}^i(t)\right) \cdot \boldsymbol{Q}^i(t) \tag{S14}$$

$$\bar{\boldsymbol{v}}_j(t + \delta t) = \bar{\boldsymbol{v}}_j(t) + \delta t \cdot \frac{d\bar{\boldsymbol{v}}_j}{dt}\left(t + \frac{\delta t}{2}\right) \tag{S15}$$

$$\boldsymbol{\omega}^i(t + \delta t) = \boldsymbol{\omega}^i(t) + \delta t \cdot \frac{d\boldsymbol{\omega}^i}{dt}\left(t + \frac{\delta t}{2}\right) \tag{S16}$$

$$\bar{\boldsymbol{x}}_j(t+\delta t) = \bar{\boldsymbol{x}}_j\left(t+\frac{\delta t}{2}\right) + \frac{\delta t}{2}\cdot \bar{\boldsymbol{v}}_j\left(t+\delta t\right) \tag{S17}$$

$$\boldsymbol{Q}^i(t+\delta t) = \exp\left[\frac{\delta t}{2}\boldsymbol{\omega}^i\left(t+\frac{\delta t}{2}\right)\right]\cdot \boldsymbol{Q}^i\left(t+\delta t\right) \tag{S18}$$

where $j \in [0, n]$ and $i \in [0, n-1]$. Discrete energies are given in [2].

For more information about the physical model and simulation scheme used, see [2].

C. Stress-strain Relation Validation and Plasticity

We compare the maximum local strains exhibited in our simulations to experimentally determined and theoretically modeled stress-strain curves for materials with a comparable Young's modulus to the one used in simulation. For all simulations except those used in Fig. S7, S4, S5 and Fig. 4c of the main text, we set Young's modulus to 1 MPa, so we compare the maximum strains of those simulations to the stress-strain curves of rubber. The authors of [8, 9] show that uniaxial extension is reversible to at least 350% strain, well above the maximum local strain obtained by any simulation with $E = 10^6$ MPa. Since our simulations lie in the purely elastic regime, we validate our model by comparison to Neo-Hookean and Mooney-Rivlin hyperelastic models. Referring to Appendix B of [2], our model's stress-strain relations fall between Neo-Hookean and Mooney-Rivlin models and remain close to both through 130% strain, the highest achieved by any rubber simulation used in the main text (Fig. S3).

We report maximum values for two types of strain in all rubber simulations: the local extension of one hemisphere of adjoining cross-sections due to bending and stretching, and the pure extension of the centerline due to stretching. We compute the former via $\epsilon_{\text{local}} = e - 1 + e\tilde{a}\sqrt{k_1^2 + k_2^2}$, where ϵ_{local} is the extension of one side of a set of adjacent cross-sections, e is the local dilatation, $\tilde{a}$ is the deformed filament radius and k_i is the ith component of the curvature vector in the material frame and with respect to the deformed arc-length.

Using this metric, we find following maximum values of $|\epsilon_{\text{local}}|$ and $e-1$:

TABLE S1: Max strain values (rubber simulations)

Simulations	$\lvert\epsilon_{\text{local}}\rvert$	$e-1$
Fig. 2,3 (plectonemes)	1.15	0.23
Fig. 2,3 (solenoids)	1.29	0.25
Fig. 4a	1.19	0.25
Fig. 4b	1.20	0.23
Fig. S7	2.10	0.41
Fig. S6	1.57	0.31

We note that Fig. S6 and S7 have a maximum $|\epsilon_{\text{local}}|$ greater than 130%, but for Fig. S7 we use a smaller E, so the comparison to rubber is less meaningful; we include this simulation to show that stretch, rather than shear, is critical for solenoid formation. Similarly, we include Fig S6 simply to demonstrate the qualitative effects of boundary conditions on solenoid formation.

Since the maximum extension and local strain due to bending and stretching are both within the regime of reversible pure elasticity and our model gives stress-strain relations comparable to a combination of Mooney-Rivlin and Neo-Hookean hyperelastic models, we conclude that our model is sufficient for full qualitative and even accurate quantitative comparisons of the rubber simulations and experiments discussed here.

To simulate nylon, we use $E = 30$ GPa [10, 11] and try modeling nylon with and without plasticity [19]. To replicate plasticity, we allow Young's modulus to depend on strain. Following the stress-strain curves of [10, 11], we irreversibly reduce the local Young's modulus (for a discretized rod the local Young's modulus affects the stretch/shear matrix over a single edge and bending/twist matrix over a single internal node Voronoi domain) by 90% when the local extension of one hemisphere of adjoining cross-sections due to bending and stretching (defined below) exceeds 0.15. We show the results of simulating twisted and coiled polymer muscles without plasticity (Fig. 4b of main text) and with plasticity (Fig. S4). Since there is little quantitative difference between the two simulations, we neglect plasticity in the main text, leading to a simpler model. Note that in both of these simulations, the filament is annealed into a helical rest configuration early in the numerical experiment. Plasticity irreversibly and uniformly changes the Young's modulus of the entire filament as it is bent before annealing. However, after annealing the maximum strains due to bending and stretching (0.041, measured with respect to the new helical rest configuration of the filament) remain well below the plasticity threshold of 0.15.

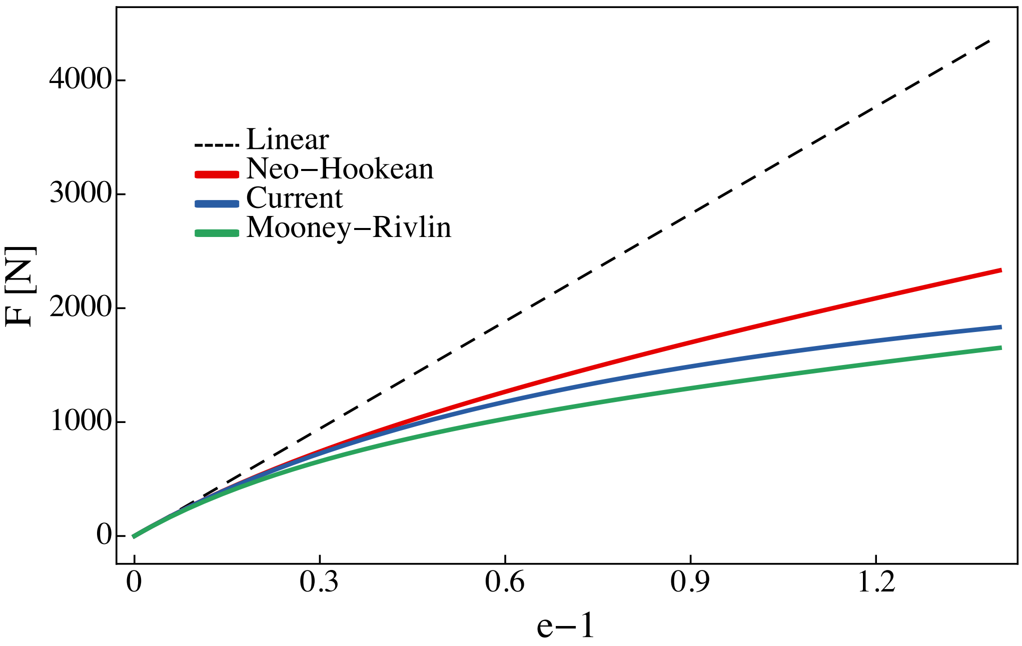

FIG. S3: Axial stretch comparison with Neo-Hookean and Mooney-Rivlin models [2]. Stress-strain curves as predicted by our model and hyperelastic Mooney-Rivlin and Neo-Hookean models. Stress-strain curves are predicted using $F_{\text{Neo-Hookean}} = 2C_{10}A\left(e - \frac{1}{e^2}\right)$, $F_{\text{M-R}} = \frac{A}{e}\left(2C_{10}\left(e^2 - \frac{1}{e}\right) + 2C_{01}\left(e^2 - \frac{1}{e}\right)\frac{1}{e}\right)$ and our model gives $F = \frac{A}{e}E\left(e - 1\right)$. We use $C_{10} = E/6$ for the Neo-Hookean model and $C_{10} = C_{01} = E/12$ for Mooney-Rivlin, with E here denoting the low-strain Young's modulus. We take $A = \pi \cdot 0.025^2$, since $a = 0.025$ for most rubber simulations.

S2. KNOT THEORY CALCULATIONS

We model the filament as an open ribbon. We define our ribbon by the curve $\bar{\boldsymbol{x}}(s)$ and normal vectors $\bar{\boldsymbol{d}}_1^{\perp}(s)$ (i.e. $\bar{\boldsymbol{d}}_1(s)$ projected onto the normal-binormal plane of $\bar{\boldsymbol{x}}_s$). We define an auxiliary curve $\bar{\boldsymbol{a}}(s)$ as the path traced out by $\bar{\boldsymbol{d}}_1^{\perp}(s)$ once $\bar{\boldsymbol{d}}_1^{\perp}(s)$ is translated pointwise by $\bar{\boldsymbol{x}}(s)$ and normalized to the filament radius a. $\bar{\boldsymbol{a}}(s)$ is shown in red in simulated filament images (the corresponding curve associated with $-\bar{\boldsymbol{d}}_1$ is shown in yellow).

To compute link, writhe and twist of the ribbon we draw on methods from [12]. To compute writhe and link, we apply "Method 1a" from [12]. Since writhe is the link of a curve with itself, we will describe here only the computation of link.

We append to the centerline two edges: one extending from $\bar{\boldsymbol{x}}_0$ to $\bar{\boldsymbol{x}}_0 + \alpha L_0 \boldsymbol{d}$ and another from $\bar{\boldsymbol{x}}_n$ to $\bar{\boldsymbol{x}}_n - \alpha L_0 \boldsymbol{d}$, where $\alpha \gg 1$ and $\boldsymbol{d}$ is a roughly axial direction pointing from the bottom toward the top of the filament. For all rubber simulations (Fig. 2, 4a, 4b, S2, S8, S7, S6) we use $\boldsymbol{d} = \frac{\bar{\boldsymbol{x}}_0 - \bar{\boldsymbol{x}}_n}{|\bar{\boldsymbol{x}}_0 - \bar{\boldsymbol{x}}_n|}$, and for nylon simulations (Fig. 4c, S4, S5) we use $\boldsymbol{d} = \frac{\boldsymbol{m}_{\text{c,top}} - \boldsymbol{m}_{\text{c,bot}}}{|\boldsymbol{m}_{\text{c,top}} - \boldsymbol{m}_{\text{c,bot}}|}$, where $\boldsymbol{m}_{\text{c,top}}$ is the pointwise average (in this case agreeing with the center of mass) of node coordinates $\{\bar{\boldsymbol{x}}_i\}_{i=0}^{\lfloor (n-1)/2 \rfloor}$ and $\boldsymbol{m}_{\text{c,bot}}$ is the center of mass of node coordinates $\{\bar{\boldsymbol{x}}_i\}_{i=\lceil (n-1)/2 \rceil}^{n}$. We use $\alpha = 10$, empirically determined as sufficiently large to make trivial any discrepancy in the CFW theorem coming from the centerline and auxiliary curves' open ends. We also append a similar pair of two edges to the auxiliary curve $\bar{\boldsymbol{a}}(s)$, extending axially away from each end of the auxiliary curve a distance αL_0. We henceforth use $\bar{\boldsymbol{x}}(s)$ and $\bar{\boldsymbol{a}}(s)$ to refer to the curves including these additional edges.

We compute the link between all individual pairs of edges $(\bar{\boldsymbol{e}}_i, \bar{\boldsymbol{e}}_j)$, where $\bar{\boldsymbol{e}}_i$ is taken from $\bar{\boldsymbol{x}}(s)$ and $\bar{\boldsymbol{e}}_j$ from $\bar{\boldsymbol{a}}(s)$. We sum the contributions from all pairs to obtain the total link between $\bar{\boldsymbol{x}}(s)$ and $\bar{\boldsymbol{a}}(s)$:

$$Lk = \sum_{i=0}^{n+1} \sum_{j=0}^{n+1} Lk(\bar{\boldsymbol{e}}_i, \bar{\boldsymbol{e}}_j) \tag{S19}$$

Note that the sum runs over $n+2$ edges in each curve, corresponding to n physical edges and two additional edges.

We define $Lk(\bar{\boldsymbol{e}}_i, \bar{\boldsymbol{e}}_j) = \frac{1}{4\pi}\Omega_{i,j} = \frac{1}{4\pi}\epsilon_{i,j}\Omega^*_{i,j}$, where $\epsilon_{i,j} = \pm 1$. $\Omega^*_{i,j}$ is the solid angle of view directions from which $\bar{\boldsymbol{e}}_i$ and $\bar{\boldsymbol{e}}_j$ appear to intersect, with $\bar{\boldsymbol{e}}_i$ closer to the viewpoint. We can compute this solid angle consistently by looking at the four rays emanating from the endpoints of $\bar{\boldsymbol{e}}_j$ and passing through the endpoints of $\bar{\boldsymbol{e}}_i$. We take four new rays which originate at the center of our unit sphere and are parallel to the aforementioned rays. The intersection points of these four new rays with the unit sphere form the apexes of the desired solid angle. If the oriented edges $\bar{\boldsymbol{e}}_i$ and $\bar{\boldsymbol{e}}_j$ appear to form a right-handed intersection $\epsilon_{i,j} = 1$; otherwise $\epsilon_{i,j} = -1$. See Method 1a in [12] for details.

Since writhe is the link of the filament centerline with itself, we evaluate writhe using the same method as link, summing over all pairs $(\bar{\boldsymbol{e}}_i, \bar{\boldsymbol{e}}_j)$ where now both segments come from $\bar{\boldsymbol{x}}(s)$. Note that writhe is multiplied by an implicit factor of 2 compared with link, coming from summing (or in smooth curves, integrating) over the same curve twice.

To compute twist, we adapt techniques from "Method 2a" in [12]. Note that the additional unphysical edges used to compute link and writhe are irrelevant to computation of twist. Thus we revert back to using $\bar{\boldsymbol{a}}(s)$ and $\bar{\boldsymbol{x}}(s)$ to refer to the physical centerline and auxiliary curves (i.e. without any additional edges).

We associate to each vertex $\bar{\boldsymbol{x}}_i$ the vector $\bar{\boldsymbol{a}}_i = \bar{\boldsymbol{a}}(s = L_0 i/n) - \bar{\boldsymbol{x}}_i$. For $i \in 1, ..., n$, we define $\bar{\boldsymbol{a}}_i$ as $\bar{\boldsymbol{d}}_1^{i-1}$ projected onto the plane perpendicular to $\bar{\boldsymbol{e}}^{i-1}$ and normalized to have length equal to the filament radius a. We define $\bar{\boldsymbol{a}}_0$ as $\bar{\boldsymbol{d}}_1^0$ projected onto the plane perpendicular to $\bar{\boldsymbol{e}}^0$ and normalized to a. For each pair of sequential normal vectors $(\bar{\boldsymbol{a}}_i, \bar{\boldsymbol{a}}_{i+1})$ we compute the angle of rotation needed to rotate $\bar{\boldsymbol{a}}_i$ into $\bar{\boldsymbol{a}}_{i+1}$. For each pair, this rotation has two steps: one rotation around $\bar{\boldsymbol{e}}^{i-1}$ (the edge perpendicular to $\bar{\boldsymbol{a}}_i$) and another rotation around $\bar{\boldsymbol{e}}^i$ (the edge perpendicular to $\bar{\boldsymbol{a}}_{i+1}$). Note that $\bar{\boldsymbol{a}}_0 = \bar{\boldsymbol{a}}_1$, so this pair does not contribute to the total twist.

To compute these two rotations for each pair of vectors, we define a new set of vectors $\bar{\boldsymbol{p}}^i$ such that $\bar{\boldsymbol{p}}^i$ is the unique vector of length a in the direction $\bar{\boldsymbol{e}}^{i-1} \times \bar{\boldsymbol{e}}^i$. If $\bar{\boldsymbol{e}}^{i-1}$ and $\bar{\boldsymbol{e}}^i$ are parallel, we can take $\bar{\boldsymbol{p}}^i$ in an arbitrary direction. Note that we define one vector $\bar{\boldsymbol{p}}_i$ for each interior vertex. Then we can compute the minimal rotation α_i about $\bar{\boldsymbol{e}}^{i-1}$ needed to transform $\bar{\boldsymbol{a}}_i$ into $\bar{\boldsymbol{p}}_i$ and the minimal rotation γ_i about $\bar{\boldsymbol{e}}^i$ needed to transform $\bar{\boldsymbol{p}}_i$ into $\bar{\boldsymbol{a}}_{i+1}$. The contribution to the total twist coming from the pair $(\bar{\boldsymbol{a}}_i, \bar{\boldsymbol{a}}_{i+1})$ is $\alpha_i + \gamma_i$. Finally, we sum these individual contributions to obtain the total twist

$$Tw = \frac{1}{2\pi}\sum_{i=1}^{n-1}(\alpha_i + \gamma_i) \tag{S20}$$

Note that this method assumes all individual contributions $\frac{1}{2\pi}(\alpha_i + \gamma_i) \in [-1/2, 1/2]$. See [12] for details.

Note that the knot theory Calugareanu-Fuller-White (CFW) theorem and the above knot theoretic computation techniques apply to closed ribbons; we applied them to open filaments and showed that the CFW theorem holds up to a vanishingly small error. We adjusted the length of the additional edges appended to $\bar{\boldsymbol{x}}(s)$ and $\bar{\boldsymbol{a}}(s)$ and found that the discrepancy in the CFW theorem (i.e. $Link$ - $(Wr + Tw)$) asymptotes to a small value on the order of $10^{-6} \cdot Link$, as the length of the additional segments becomes large compared to L_0. For the simulation shown in Movie S2 (described in figure 2b of our article) for which we compute link and writhe using additional edges of lengths $\approx 10L_0$ as described above, $sup[Lk - (Tw + Wr)] \approx 6.4 \cdot 10^{-5}$. We conclude that for the deformations considered here, artificially extending the centerline and auxiliary curve suffices to allow meaningful application of the CFW theorem.

S3. SIMULATION SETTINGS

For all simulations except that referenced by Fig. S7, S4, S5 and Fig. 4b in the main text, we use:

TABLE S2: Simulation settings (except Fig. S4, S5, S7, S10, 4b main text):

L_0	1 m
rest state radius a	$0.025L_0$
Young's modulus E	1 MPa
shear modulus G	$2E/3$
shear/stretch matrix $\boldsymbol{S}$	$\mathrm{diag}(4GA/3, 4GA/3, EA)$ N
bending/twist matrix $\boldsymbol{B}$	$\mathrm{diag}(EI_1, EI_2, GI_3)$ Nm^2
discretization elements n	100
mass line density ρA	1 kg/m

TABLE S3: Fig. S7 settings (where different from above)

Young's modulus E	0.1 MPa
shear modulus G	$2E/3$
shear/stretch matrix $\boldsymbol{S}$	$\mathrm{diag}(500(4GA/3), 500(4GA/3), EA)$ N
bending/twist matrix $\boldsymbol{B}$	$\mathrm{diag}(EI_1, EI_2, GI_3)$ Nm^2

Note that in Fig. 4b (main text) and S2, $E = 1$MPa initially but increases gradually throughout the simulation. External dissipation constant γ and time step δt vary across simulations, as described below.

Note that in Movies S11 and S12 we use the same settings as in table S2 above, except $L_0 = 1.5m$.

See Fig. S10 caption for settings used in torsional actuation simulations.

Nylon simulation parameters (Fig. S4, S5 and Fig. 4b main text)

As described in the main text, we replicate anisotropic expansion-induced untwist by increasing filament rest configuration radius a while modifying the third component of curvature k_3 to keep $a \cdot Tw/L = ak_3$ constant, where Tw is the integrated twist over the filament and L is filament length.

Note that to manipulate curvature and twist $\boldsymbol{k}$, we must introduce an intrinsic curvature and twist vector $\hat{\boldsymbol{k}}$, which defines the curvature and twist of the filament in its rest configuration. We then follow [2] and replace $\boldsymbol{k}$ with $\boldsymbol{k} - \hat{\boldsymbol{k}}$ in all governing equations. We then manipulate $\hat{k}_3$ to make $a\hat{k}_3$ constant, producing an elastic torque on the filament whenever ak_3 starts to change. To replicate muscle actuation experiments in Baughman, we use the formula from Love [4] for contraction of a coil due to untwist:

$$\Delta U = \frac{L_0 \Delta Tw}{N}$$

where U is coil length, Tw is twist integrated over the filament, and N is number of coil loops. We define $\Delta Tw = Tw - Tw_0$ to be the change in Tw from its initial value Tw_0. Note that for simple coil contraction with no load, $L \approx L_0$ throughout the contraction process. In terms of initial helix radius R_0 and initial helix pitch P_0, the relative change in coil length due to change in twist density is

$$\frac{\Delta U}{U_0} = \left(\frac{4\pi^2 R_0^2}{P_0} + P_0 \right) \frac{\Delta Tw}{L_0}$$

To reproduce Baughman's actuation experiment, we wish to simulate a coil with a similar value of $\left(\frac{4\pi^2 R_0^2}{P_0} + P_0 \right)$ to that in Fig. 2 of [7]. Since the coil used in [7] is microscopic, we instead simulate a precisely scaled larger helix and compare the scaled contraction of our helix to that in [7]. In particular, since $\left(\frac{4\pi^2 R_0^2}{P_0} + P_0 \right) = 0.00784$ in [7], we choose a helix with $\left(\frac{4\pi^2 R_0^2}{P_0} + P_0 \right) = 0.00784\alpha$ and compare Baughman's contraction $\Delta U/U_0$ as a function of untwist $\Delta Tw/L_0$ to our contraction as a function of scaled untwist $\alpha \Delta Tw/L_0$ (Fig. 4b of the main text).

In each nylon contraction simulation, we first choose initial and final values of a, and choose $P_0 > 2a_0$ to leave space between adjacent loops. To satisfy $\left(\frac{4\pi^2 R_0^2}{P_0} + P_0 \right) = 0.00784\alpha$ we set $L_0 = N\sqrt{0.00784\alpha P_0}$. Finally, to satisfy arc-length conservation for an unstretched helix, we set $R_0 = \sqrt{L_0^2 - N^2 P_0^2}/(2\pi N)$. We initialize the filament with a nonzero intrinsic twist density, and then anneal the filament into the specified helix shape.

To select a P_0 which gives a desired untwist density $\Delta Tw/L_0$ before self-contact begins, we consider the changes in deformed filament radius $\tilde{a}$ and deformed helix pitch P with respect to untwist ΔTw. However, as noted above, for simple coil contraction there is no extension of the underlying filament to speak of, so we can approximate $\tilde{a} \approx a$. Using this approximation, when $P = 2a$, self-contact begins. To keep ak_3 constant, $a = \frac{a_0 Tw_0}{Tw_0 + \Delta Tw}$ where a_0 is the initial filament rest configuration radius [20]. From Love's formula relating untwist to coil contraction, we find $P = P_0 + \left(4\pi^2 R_0^2 + P_0^2\right) \Delta Tw/L_0$. We assume helix radius R remains approximately constant, so that we can set $R = R_0$. Setting $P = 2a$, we find that self-contact begins at

$$\Delta Tw_{\text{contact}} = -\frac{L_0 P_0 + P_0^2 Tw_0 + 4\pi^2 R_0^2 Tw_0 - \sqrt{\left(L_0 P_0 + Tw_0\left(P_0^2 + 4\pi^2 R_0^2\right)\right)^2 - 4 L_0 Tw_0 (P_0 - 2a_0)\left(P_0^2 + 4\pi^2 R_0^2\right)}}{2\left(P_0^2 + 4\pi^2 R_0^2\right)}$$

For a given initial intrinsic twist density Tw_0, we can use this to solve for the pitch P which would lead to self-contact at a given twist density. In particular, for the contraction simulations performed here, we have

$$L_0 = N\sqrt{\alpha 0.00784 P_0} \quad R_0 = \frac{\sqrt{L_0^2 - P_0^2 N^2}}{2N\pi}$$

If we further write $Tw_0 = \rho_0 L_0$ and $\Delta Tw = \rho_\Delta L_0$, then the initial helix pitch for which self-contact will begin at the untwist density ρ_Δ is

$$P_0 = \frac{2a_0\rho_0}{(\rho_\Delta + \rho_0)(1 + 0.00784\alpha\rho_\Delta)}$$

We use the formula above to solve for $P_0 \approx 0.056$ which should lead to self-contact onset at the same relative untwist $\Delta Tw/L_0 \approx -0.62$ as that seen in the experiments of [7]. We show simulation results for this P in Fig. 4b of the main text, and for this P and twice this P in Fig. S4.

For the simulations in Fig. S4, S5 and Fig. 4c of the main text, we set $a = 0.01$ initially and grow until $a = 0.02$, and use an uniform initial intrinsic twist density of 2 rot/m (Fig. S4, 4c main text) or -2 rot/m (Fig. S5). We set the mass line density to 20 kg/m, and construct $\boldsymbol{S}$ and $\boldsymbol{B}$ as in Fig. 2, 3, 4a and 4b of the main text (see table above).

As described above, to approximate the material properties of nylon, we set $E = 30$ GPa [10, 11] and try simulating with and without plasticity. We set the Poisson ratio to 0.5 since the equations of motion are derived assuming incompressible material, and hence use $G = 2E/3$. The true Poisson ratio for nylon is slightly smaller but this parameter does not impact the contraction and expansion results of Fig. 4c, S4 and S5 since we directly control the radial and axial expansion of the filament to mimic heat-induced anisotropic expansion.

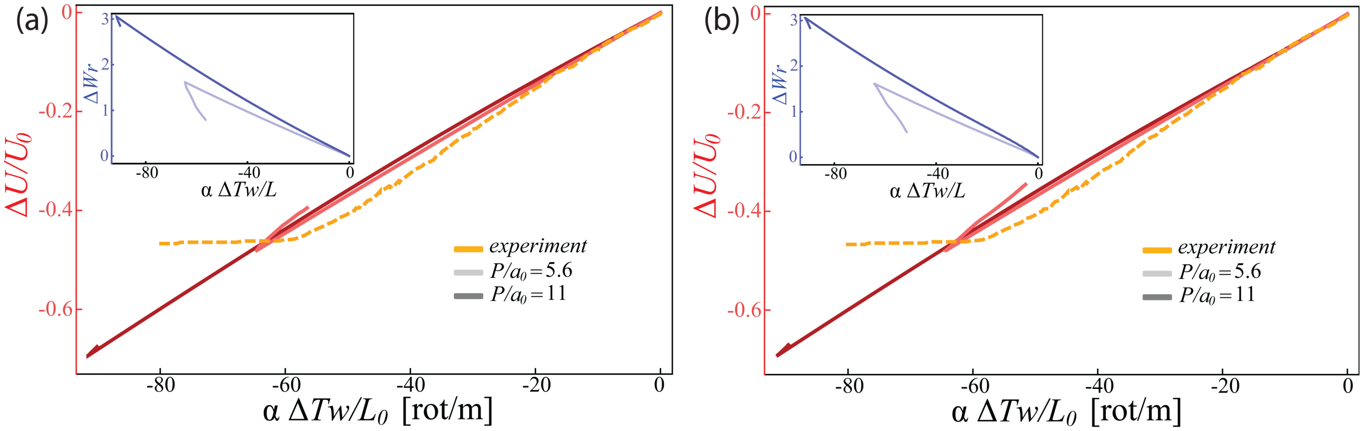

FIG. S4: Contraction of twisted and coiled nylon polymer muscle with and without plasticity. We reproduce Fig. 4c from the main text now modeling the nylon filament with **(a)** a strain-dependent Young's modulus to allow for plasticity and **(b)** no plasticity (as in Fig. 4c main text). Here we show simulation results past the onset of self-contact and for two different initial pitches. To simulate plasticity, we decrease the local Young's modulus by 90% when the local strain due to bending and stretching exceeds 15%, in approximate accordance with the results of [10, 11]. As in Fig. 4c, the filament is given an initial inserted twist density of 2 rot/m and numerically annealed into a helix with pitch P. Filament radius double from an initial radius $a_0 = 0.01$ m while intrinsic twist density decreases to keep ak_3 constant. Untwist leads to greater writhe Wr and hence coil contraction, until self-contact begins at which point radial expansion dominates leading to retwisting and expansion of the coil. Note that link escapes the system throughout due to revolution of the bottom filament endpoint around the helix axis, reducing the number of loops in the helix and leading to lower writhe during retwisting than initial untwisting. Numerical slope and onset of self-contact for $P = 0.056$ m agree closely with experimental results [7]. In addition, larger initial pitch leads to more untwist and contraction before self-contact, in agreement with the discussion in [7]. Since accounting for plasticity causes almost no quantitative difference in simulation results, we conclude that the simpler purely elastic model is sufficient to understand solenoid contraction. See Movies S4, S5. Simulation settings (see section S3): E=30 GPa, G=$2E/3$, $\boldsymbol{S}$=diag$(4GA/3, 4GA/3, EA)$ N, $\boldsymbol{B}$=diag(EI_1, EI_2, GI_3) Nm^2. Note that pitch P, $\alpha = 100$, number of loops and helix radius determine L_0.

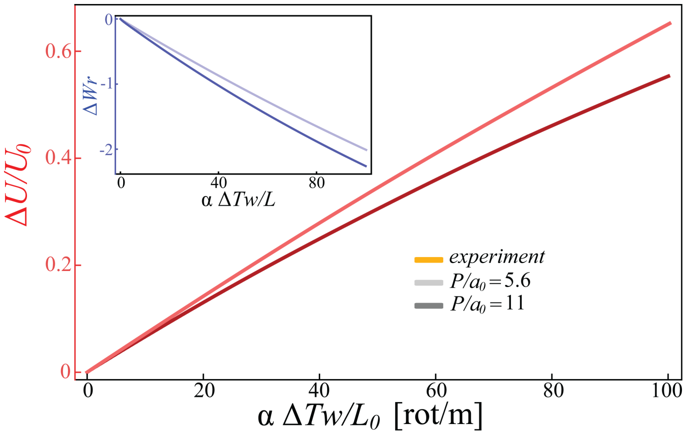

FIG. S5: Expansion of twisted and coiled nylon polymer muscle. A filament with initial inserted twist density of -2 rot/m is numerically annealed into a heterochiral helix with pitch P. Filament radius double from an initial radius $a_0 = 0.01$ m while intrinsic twist density becomes less negative to keep ak_3 constant. Greater twist requires a decrease in Wr and hence pushes coils farther apart. Numerical slopes agree closely with those for contraction (Fig. S4, 4c main text), provided we scale twist density $\Delta Tw/L_0$ by $\alpha = 100$, as in Fig. S4 and 4c main text. Since plasticity had little quantitative impact on contraction, we neglect plasticity here. See Movies S6, S7. Simulation settings (see section S3): E=30 GPa, G=$2E/3$, $\boldsymbol{S}$=diag$(4GA/3, 4GA/3, EA)$ N, $\boldsymbol{B}$=diag(EI_1, EI_2, GI_3) Nm^2. Note that pitch P, $\alpha = 100$, number of loops and helix radius determine L_0.

Energy dissipation

We introduce a linear internal energy dissipation mechanism not included in the original simulation framework of [2]. We add terms to the linear and angular momentum balance equations of the forms $\partial_s \left(\boldsymbol{Q}^T \tilde{\boldsymbol{S}} \partial_t \boldsymbol{\sigma}/e \right)$ and $\partial_s \left(\tilde{\boldsymbol{B}} \partial_t \boldsymbol{k}/e^3 \right)$, respectively, where $\tilde{\boldsymbol{S}} = \gamma_S \boldsymbol{S}$ and $\tilde{\boldsymbol{B}} = \gamma_B \boldsymbol{B}$. The internal dissipation constants γ_S and γ_B vary across simulations:

TABLE S4: Damping and time step

simulations	γ	γ_S	γ_B	δt
Fig. 2a, S1a	10 kg/ms $\approx 5.75\gamma_{\text{char}}$	0	0	$0.0025\delta l$
Fig. 2b, S1b	15 kg/ms $\approx 8.62\gamma_{\text{char}}$	0	0	$0.0012\delta l$
Fig. 3	2 kg/ms $\approx 1.15\gamma_{\text{char}}$	0	0	$0.01\delta l$
Fig. 4a	1 kg/ms $\approx 0.57\gamma_{\text{char}}$	0.12	0	$0.001\delta l$
Fig. 4b	6 kg/ms $\approx 3.45\gamma_{\text{char}}$	0.001	0.001	$0.0025\delta l$
Fig. 4c, S4, S5	2 kg/ms $\approx 0.16\gamma_{\text{char}}$	0.2	0.05	$0.0025\delta l$
Fig. S8	6 kg/ms $\approx 3.45\gamma_{\text{char}}$	0	0	$0.0025\delta l$
Fig. S7	11 kg/ms $\approx 20.0\gamma_{\text{char}}$	0.00545	0.37	$0.001\delta l$
Fig. S6	15 kg/ms $\approx 8.62\gamma_{\text{char}}$	0	0	$0.0012\delta l$
Fig. S2	6 kg/ms $\approx 3.45\gamma_{\text{char}}$	0	0	$0.0025\delta l$
Fig. S10	12.5 kg/ms $\approx 2.7\gamma_{\text{char}}$ [21]	0	0	$0.001\delta l$
Movie S11	15.0 kg/ms $\approx 19.40\gamma_{\text{char}}$	0.12	0	$0.0008\delta l$

Note that the small oscillations seen in Fig. 4a and S7 come from high frequency/short wave-length inertial modes and are irrelevant to the filament's equilibrium configurations.

In the above table,

$$\gamma_{char} = m/(L_0 \cdot t_{char}), \quad t_{char} = L_0/v_{char}, \quad v_{char} = \sqrt{F_C L_0/m} = \sqrt{\pi^2 EI/(mL_0)}, \quad \delta l = L_0/n$$

for a filament of total mass m stretched by the characteristic force $F_C = \pi^2 EI/L_0^2$, the critical compressive buckling force of an inextensible filament. Thus,

$$t_{char} = \sqrt{4mL_0^3/(Ea^4\pi^3)}\text{ seconds}, \quad \gamma_{char} = \sqrt{Ea^4\pi^3 m/(4L_0^5)}$$

S4. COMPARISON TO EXPERIMENTAL PHASE SPACE (FIGURE 3)

The experiments from reference [13] (A. Ghatak and L. Mahadevan) shown in Fig. 3 used filaments with Young's modulus $E = 1.3$ MPa and diameter $2a = 3.175$ mm (circles), $E = 1.3$ MPa and $2a = 6.35$ mm (triangles), and $E = 2.6$ MPa and $2a = 6.35$ mm (squares).

Note that the authors of [14] describe the straight-plectoneme-solenoid transition with respect to twist density. However, their experiments correspond to a combination of horizontal and diagonal paths through Fig. 3. In particular, they begin with a highly stretched and untwisted filament (e.g. a point such as $L/L_0 = 1.2$, $\Phi a = 0$). They twist the filament, keeping the ends fixed in space, until a little below the straight-solenoid transition (e.g. $L/L_0 = 1.2$, $\Phi a = 1.4$). Now they let the filament contract while keeping the end frames fixed, moving toward lower L/L_0 at fixed Φa and crossing the straight-solenoid transition line, ending in the solenoid region, for example around $L/L_0 = 1.15$, $\Phi a = 1.4$. They now let the solenoid contract further, again decreasing L/L_0 at fixed Φa until the filament reaches the solenoid-plectoneme transition line (e.g. $L/L_0 = 1.11$, $\Phi a = 1.4$). They note that the solenoid is unstable here, and proceed to increase the twist. However, as shown in Fig. S6, twisting a filament with fixed ends causes an increase in stretch as well due to filament looping. Hence, this step sends the filament on a steplike path in a generally diagonal direction of greater L/L_0 and greater Φa. As can be seen from Fig. 3, this path leads back into the solenoid phase, to a point such as $L/L_0 = 1.12$, $\Phi a = 1.6$). They again let the solenoid contract, moving toward lower L/L_0 at fixed Φa and heading back toward the solenoid-plectoneme transition line.

We note that for an initially straight and untwisted filament with fixed ends, twisting can indeed send the filament into first a plectoneme and then a solenoid phase, since buckling with fixed-end boundary conditions requires stretching. Hence, were a filament to begin at point with both L/L_0 and Φa lower than their values at the triple point, twisting with fixed ends could send the filament on a step-like diagonal path first into the plectoneme regime, and then (moving toward higher stretch and twist) into the solenoid regime. Such an experiment relies on but might not capture the fact that L/L_0 determines the filament's buckled state at any twist density for which a straight filament is not stable.

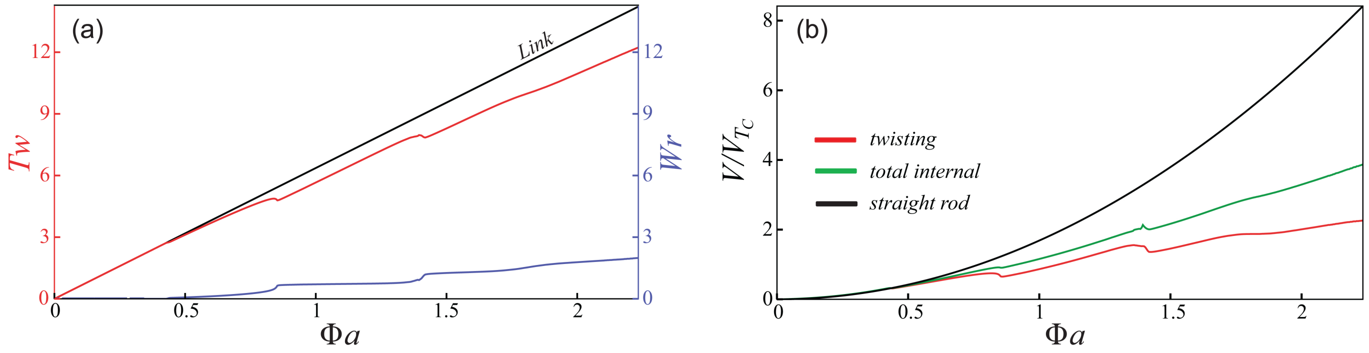

FIG. S6: We simulate a twisting experiment similar to those in Fig. 2 but with modified boundary conditions. We clamp the filament's top and bottom vertices a constant distance L_0 and clamp the top frame. We twist the bottom frame axially but require it to remain oriented vertically (i.e. parallel to $\bar{\boldsymbol{x}}_0 - \bar{\boldsymbol{x}}_n$). **(a)** We show link, twist and writhe over dimensionless twist density of an equivalently twisted straight filament. **(b)** We show twisting and total internal energy of the filament and the theoretical total energy of an equivalently twisted straight filament, all over dimensionless twist density. Energies (V) are plotted relative to V_{T_C} (see Fig. S1 caption). Note that bending subject to these boundary conditions requires stretching, and forming the first loop stretches the filament into the solenoidal regime. As in Fig. 2b and S7, the solenoid converts twist to writhe in a step-like process. However, modifying the boundary conditions changes the set of stable equilibrium configurations leading to a qualitatively new deformation process. See Movie S8.

Finally, we confirm that it is stretch, rather than shear, that is essential for solenoid formation. Hence we are justified in considering only extension and twist, neglecting shear, when studying the filament phase space. In particular, in Fig. S7, we form a solenoid despite increasing the filament shearing rigidity by a factor of 500 greater than that normally used for incompressible material. As seen in Fig. S7, increasing shear rigidity does quantitatively modify the exact steplike transitions inherent to solenoid formation, but does not affect the final result: a twisted filament with sufficient extension will buckle into a solenoid even if it is hardly able to shear.

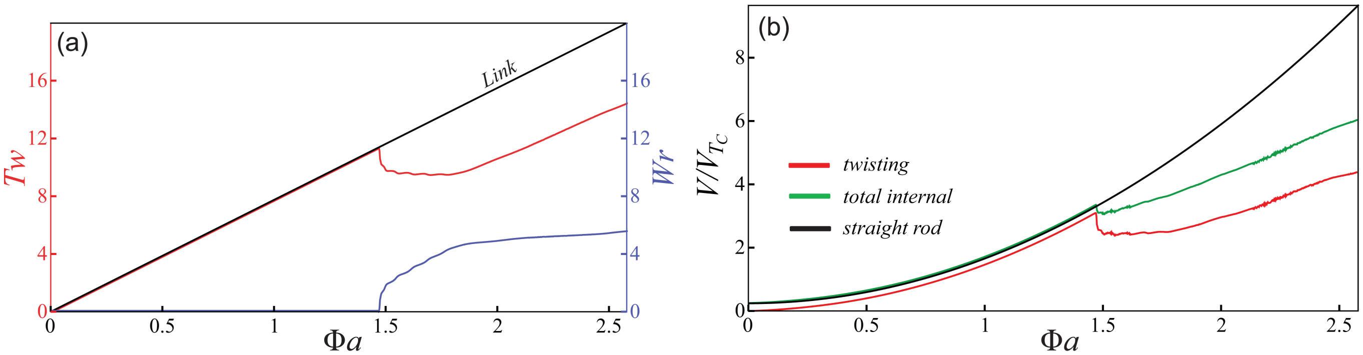

FIG. S7: We simulate a twisting experiment as in Fig. 2b, now using a constant 35 N $\approx 116F_C$ axial load, lowering Young's modulus to $E = 0.1$ MPa, keeping $G = 2E/3$ and increasing only shear rigidity with rigidity matrices $\boldsymbol{S} = \mathrm{diag}(500(4GA/3), 500(4GA/3), EA)$ N and $\boldsymbol{B} = \mathrm{diag}(EI_1, EI_2, GI_3)$ Nm^2. **(a)** We plot twist, writhe and link over dimensionless twist density Φa of an equivalently twisted straight filament. **(b)** We plot twisting and total energy of our filament and the theoretical total energy of an equivalently twisted straight filament. Energies (V) are plotted relative to V_{T_C}, defined as in Fig. S1 caption, where we again compute V_{T_C} assuming an axial load $F \approx 41F_C$, which is now 12.5 N since the filament stiffness is now $E = 0.1$ MPa. As evidenced quantitatively by the multiple bumps in the twist, writhe and energy curves and qualitatively by Movie S7, this extensible but highly unshearable filament still forms a solenoid rather than a plectoneme under sufficiently high extension, reaffirming that extension, rather than shear, is the crucial prerequisite for solenoid formation. See Movie S9.

S5. LOSS OF LINK

The boundary conditions used in simulating all plectonemes and solenoids maintain a fixed orientation of both filament endpoints. Hence, twist cannot escape the filament. However, for sufficiently buckled filaments, we found that link *can* escape the system in the form of writhe. In particular, for high buckled plectonemes, as ever greater twist is inserted through the bottom end, the plectoneme axis rotates around the end-to-end axis, while the plectoneme loops take up ever more of the filament. When the first plectoneme loop gets close enough to the top (clamped end) of the filament, it flips over the top, releasing a quantum of link and reforming into a slightly less twisted plectoneme. In Fig. S8 we show the evolution of link, twist and writhe during this process. We twist the filament sufficiently to produce several of these link loss events. Note that once these events begin to occur, the link oscillates around a constant maximum value. Also note that the jump decreases in writhe in Fig. S8 occur momentarily before the jump decreases in twist: as soon as a quantum of writhe escapes, a similar amount of twist is immediately converted to writhe, converting the lost link from lost writhe to lost twist.

S6. EXPANSION OF PLECTONEME-SOLENOID MIXED STATE REGION

We find that the plectoneme-solenoid mixed state region in Fig. 3 of the main text can be expanded by controlling the position and orientation of a point in the middle of the filament to induce two segments of different tension in a single filament. In particular, we prestretch a filament by an axial load sufficient to form a solenoid under the boundary conditions of Fig. 3 of the main text. We then take inspiration from plectoneme loop extrusion in DNA [15–17], replicating loop extrusion by two different methods which we show produce nearly equivalent results. Both methods ultimately lead to plectoneme and solenoid coexistence in a region of phase space normally dominated by purely solenoidal buckling.

In the first method (see Movie S11), after prestretching the filament, we choose two points along the filament, one near the top clamped end and the other in the middle, and displace the latter towards the former, as might be driven by a large DNA binding enzyme such as the Lac-operon. This displacement relaxes the tension in the filament and eventually compresses the segment between the two points, causing it to buckle. When the free end of the filament is twisted further, the buckled segment to form a plectoneme. If we continue twisting the free filament end, but preventing the twist from entering the region between the two points associated with the clamp, the twist density in

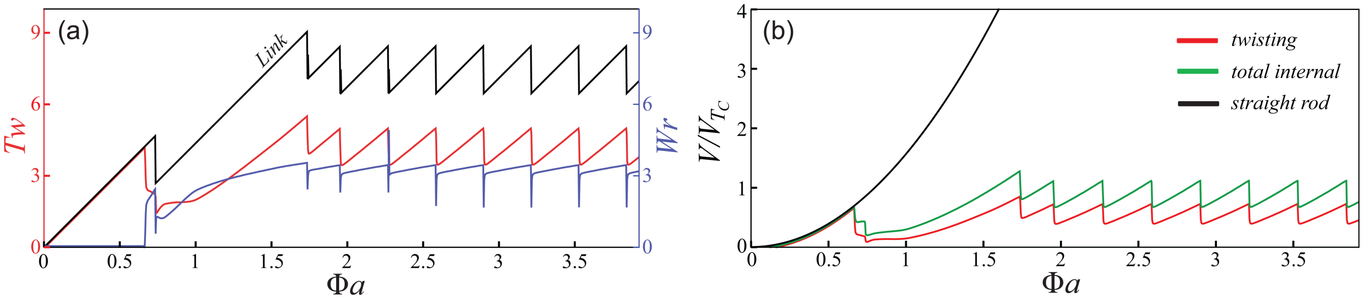

FIG. S8: We simulate a twisting experiment as in Fig. 2a from the article, now using a constant 50 N $\approx 17F_C$ axial load. **(a)** We plot twist, writhe and link over dimensionless twist density Φa of an equivalently twisted straight filament. During formation of the initial plectonemic deformation, the bottom endpoint slips through a plectoneme loop, letting link escape from the system. The plectoneme then gradually converts twist into writhe, minimizing total energy and lowering the ratio of twist to total internal energy. After reaching a critical twist density, the plectoneme deformation slips over the top endpoint of the filament, again letting link escape from the system. Twist density accumulates again, and the plectoneme loop repeatedly slips over the top endpoint, creating a sawtooth pattern. Note that $\Phi a \sim Link$ so, unlike Φa of an equivalently twisted straight filament, the twist density of our filament does not increase monotonically in this process. **(b)** We plot twisting and total energy of our filament and the theoretical total energy of an equivalently twisted straight filament. Energies (V) are plotted relative to V_{T_C} (see Fig. S1 caption). Forming a plectoneme saves energy, as does letting link escape from the system. Simulation settings: $\gamma = 6$ kg/(ms) $\approx 3.45\gamma_{char}$ and $\delta t = 0.0025\delta l$. See Movie S10.

the lower stretched filament segment crosses a critical threshold and this segment buckles out of the plane, forming solenoidal loops. As seen in Movie S11, the solenoidal loops remain somewhat unstable, traveling up and down the bottom segment of the filament dynamically. In Movie S11, we use an axial force $F = 250$ N $\approx 186F_C$.

In the second method (see Movie S12), we extrude a loop by a "feeding" mechanism, more literally similar to the extrusion mechanism observed experimentally in [15]. We again prestretch the filament by a constant axial load, but now clamp a prescribed point near the top of the filament. We then prescribe a feeding rate of the filament through this point. The end result is an extruded loop very similar to that produced by the first method above. After the loop is extruded, if we continue to insert twist through the free lower end of the filament, a plectoneme forms in the region between the feeding point and the clamped point. Further twisting of the region outside this region causes solenoidal structures to form, leading to a plectoneme-solenoid mixed state very similar to that formed in the first method.

This procedure shows that loop extrusion in a prestretched and twisted filament can expand the region of plectoneme-solenoid coexistence into the domain normally dominated by solenoids. In Fig. S9 we show the original phase boundaries of a twisted and stretched filament, and plot several mixed plectoneme-solenoid states induced by the second of the loop extrusion processes described above. We note that these mixed states formed at extensions which, without loop extrusion, would have led to solenoid formation upon further twisting, and that our induced mixed states lie mostly in the high extension part of the straight phase region because increasing twist in our extruded system sufficiently to match the twist densities seen in pure solenoids caused the system to become unstable, as can be seen at the end of movies S11 and S12.

S7. APPLICATION TO TORSIONAL/ROTARY ACTUATORS

As we were revising the current manuscript, a new paper [18] was published regarding the use of twist and coiled fiber-based artificial muscles as torsional actuators. The physical model and numerical framework we used to study filament buckling and actuation of twisted coils can also be applied to model torsional actuators. To demonstrate this, we qualitatively reproduce the twisting experiment performed in [18]. In particular, we initialize a straight filament, clamped at one end and stretched by a constant axial load at the other end. We initialize the filament in its rest state with a high intrinsic twist. We then rapidly decrease the intrinsic twist to zero, replicating the heating process by which the twisted filament in [18] was actuated. To relax elastically to its new rest state, the highly twisted filament rapidly untwists until it reaches its new zero-twist rest state. In Fig. S10 we show a filament's recovered twist angle as a function of time for two rates of decreasing intrinsic twist (i.e. two "heating" rates)—our plot is analogous to Fig. S3 in [18]. Our plots agree with experiments in [18], noting that we decrease intrinsic twist over less than two seconds—much faster than the time spent heating the experimental filaments to their programming temperature. This difference in heating causes the inflection point in our untwist curves to occur at much earlier times, as seen by comparing Fig. S10 and Fig. S3 in [18]. Indeed, as noted in [18], the inflection point in our curves and the experimental

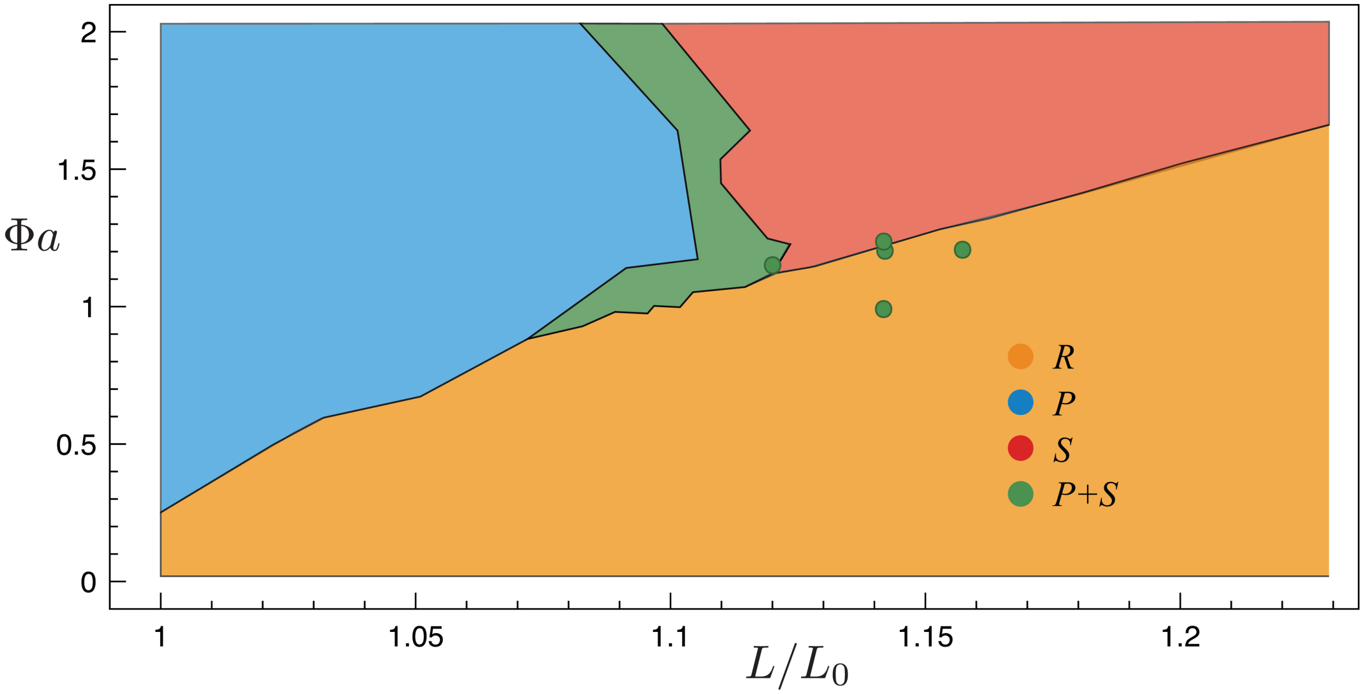

FIG. S9: We reproduce the original phase space from Fig. 3 of the main text, now showing new plectoneme-solenoid states induced by loop extrusion. Straight ("rectilinear") states are denoted by R, solenoids by S, plectonemes by P and mixed states by $P+S$. Loop extrusion allows formation of mixed states for extensions which would allow only solenoids or rectilinear states without loop extrusion. We note that mechanical instabilities at higher twist densities limits the amount of twist we can insert in forming these mixed states.

ones occurs at approximately the time at which heating is finished (i.e. for us, the time at which the intrinsic twist reaches 0; for experiments, the time at which the filament temperature reaches the programming temperature).

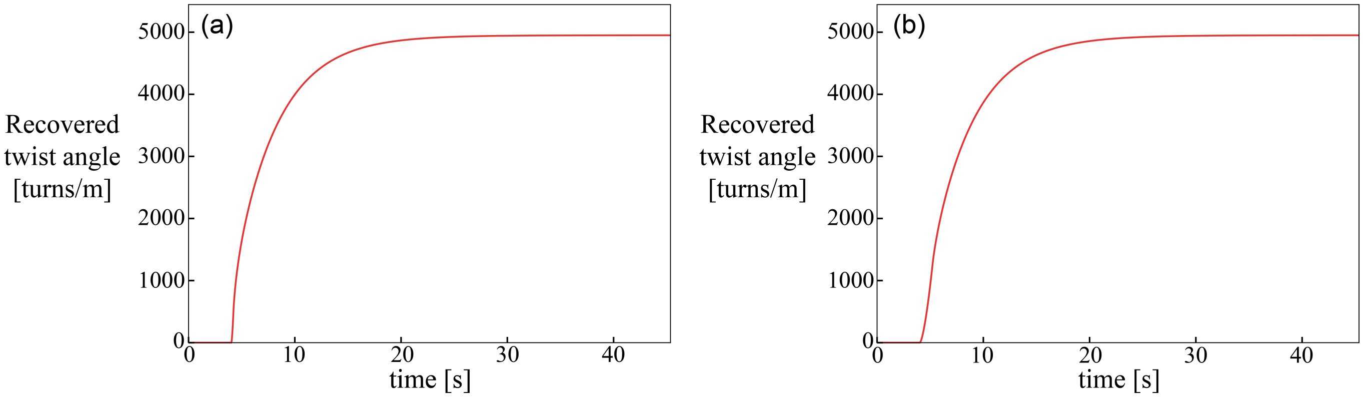

FIG. S10: Torsional actuation of twisted filament. A straight filament is initialized in its rest state with intrinsic twist 7500 turns/m. After relaxing for 4 seconds, we start decreasing the intrinsic twist to 0, completing this process in (a) 0.2 and (b) 1.2 seconds. The filament untwists as it relaxes elastically to its new rest state. The inflection point in the untwist curve occurs approximately at the time at which intrinsic twist reaches 0. Taking this moment to be equivalent to the time in [18] at which an experimental filament is heated to its programming temperature, our results agree qualitatively with experiments. Note that the maximum recovered twist angle and overall shape of the untwist curve also agrees with experiments. Filament parameters were chosen to replicate experiments on single-walled carbon nanotube-doped PVA fibers in [18]. An axial load $F = 0.7$ N $\approx 1.7 \cdot 10^4 F_C$ was applied to increase stability to buckling. Simulation settings: $E = 13.5$GPa, $G = 2.3$GPa, $\gamma = 12.5$ kg/(ms) $\approx 2.7\gamma_{\mathrm{char}}$ (see table S4), $\delta t = 0.001\delta l$, $L_0 = 0.02$ m, $a = 2 \cdot 10^{-5}$ m. See Movie S14.

S8. MOVIE CAPTIONS

Movie S1: Plectonemic deformations of a filament clamped at one end and stretched by a constant 75 N $\approx 25F_C$ axial load at the other end (Fig. 2a and Fig. S1a, see section S3 for simulation parameters).

Movie S2: Solenoidal deformations of a filament clamped at one end and stretched by a constant 270 N $\approx 90F_C$ axial load at the other end (Fig. 2b and Fig. S1b, see section S3 for simulation parameters).

Movie S3: Active actuation of a solenoidal coil (Fig. 4b and S2, see section S3 for simulation parameters). A solenoid is generated as in Movie S2, except with a constant 350 N $\approx 116F_C$ axial load. Maintaining this constant load, we gradually increase Young's modulus E from $E_0 = 1$ MPa to $E_f = 2.5E_0$. Bend and twist rigidities scale in parallel both with E and A, allowing this simulation to qualitatively reproduce the effect of heat-induced anisotropic expansion [7]. Since the simulated rubber coil is not annealed around a mandrel, new loops form to increase writhe, leading to a steplike contraction process characteristic of solenoid formation.

Movie S4: Contraction of nylon helix with inserted twist by anisotropic expansion-induced untwist. Before start of movie, the filament is given an intrinsic twist density of 2 rot/m and annealed into a helix with pitch $P = 0.056$ m. During simulation, the filament radius double from an initial $a_0 = 0.01$ m while intrinsic twist decreases to keep ak_3 constant, reproducing the anisotropic expansion-induced untwist used to activate twisted and coiled polymer muscles in [7]. Top of filament is clamped, leading to slight tilt of helix during contraction. Rate of contraction with respect to untwist density $\Delta Tw/L_0$ and untwist density at which self-contact begins agree closely with experiment [7]. After onset of self-contact, radially expansion causes the helix to elongate, forcing untwist despite an ever-decreasing intrinsic twist. Note that the free end of the filament revolves around the helix axis, reducing the number of loops in the helix and decreasing the system's total link. Plasticity is not included in the numerical model here since numerical experiments showed almost no quantitative effect from including plasticity (see Fig. S4 and Fig. 4c of the main text for comparison of models with and without plasticity, section S3 for simulation parameters).

Movie S5: Contraction of nylon helix with inserted twist by anisotropic expansion-induced untwist (Fig. S4). The same simulation procedure as in Movie S4 is used; we now set initial pitch $P = 0.11$ m (see Fig. S4, section S3 for simulation parameters).

Movie S6: Expansion of nylon helix with inserted twist by anisotropic expansion-induced untwist (Fig. S5).

The same simulation procedure as in Movie S4 is used, but here we reverse the sign of the filament's initial inserted twist density, setting the initial twist density to -2 rot/m (see Fig. S5, section S3 for simulation parameters).

Movie S7: Expansion of nylon helix with inserted twist by anisotropic expansion-induced untwist (Fig. S5). The same simulation procedure as in Movie S6 is used, but here we use initial pitch $P = 0.11$ (see Fig. S5, section S3 for simulation parameters).

Movie S8: Formation of a solenoid with both endpoints clamped a fixed distance L_0 apart. Formation of the first loop causes the filament to stretch, bringing it into the solenoid regime (Fig. S6, see section S3 for simulation parameters).

Movie S9: Formation of a solenoid in an unshearable filament (Fig. S7, see section S3 for simulation parameters).

Movie S10: Link non-conserving plectonemic deformations of a filament clamped at one end and stretched by a constant 50 N $\approx 17F_C$ axial load at the other end (Fig. S8, see section S3 for simulation parameters).

Movie S11: Mixed plectoneme-solenoid state induced in a filament with extension and twist density usually characteristic of purely solenoidal deformations. The plectoneme state is produced by replicating loop extrusion in the top half of the filament by drawing together two filament points, one near the top and the other in the middle of the filament, before twisting begins. This extrusion-like displacement of filament points creates two regions of different tensions in the filament: the top segment between the two chosen points is compressed beyond the buckling threshold while the lower segment remains stretched by the axial load. After the filament is sufficiently twisted to form a plectoneme, the orientation of the middle point is fixed so that further twisting increases the twist density only in the lower stretched segment of the filament, leading to solenoid formation in this segment. Throughout the process, the filament is clamped at the top and stretched by a constant 250 N $\approx 186F_C$ axial load at the other end.

Movie S12: We reproduce the process shown in Movie S11, this time using a "feeding" mechanism to extrude a loop. In particular, to induce planar buckling in the top part of the filament, we clamp a preselected point near the top of the filament, and prescribe an upward velocity at a point slightly lower on the filament. As the lower part of the filament translates upward, we slide the point of prescribed velocity down the filament at an equal and opposite rate to the filament's translational velocity, keeping the region through which the filament is being fed approximately fixed in lab coordinates. This method more faithfully reproduces the loop extrusion mechanism shown in [15]. However, we note that the final result is very similar to that shown in Movie S11, showing the near equivalence of the two methods in producing an extruded loop and mixed plectoneme-solenoid state.

Movie S13: Passive actuation of a solenoidal coil (Fig. 4a, see section S3 for simulation parameters). The filament is clamped at the top and subjected to a constant 300 N $\approx 99F_C$ axial load at the bottom end. The bottom end is twisted to form a solenoid, after which we displace the bottom endpoint 0.42 $L_0 = 0.42$ m away from the top endpoint.

Movie S14: Torsional actuation of a twisted filament. A filament with length $L_0 = 0.02$ m and radius $a = 2 \cdot 10^{-5}$ m is initialized in its rest state with intrinsic twist 7500 turns/m. The filament is clamped at the top and stretched by axial load $F = 0.7$ N $\approx 1.7 \cdot 10^4 F_C$ at the bottom. The filament relaxes to its stretched state for 4 seconds. We then decrease the intrinsic twist to 0 at a constant rate over a period of 1.2 seconds. To reach its new zero-twist rest state, the filament rapidly untwists, qualitatively reproducing experiments from [18]. See section S7.

---

[1] S. S. Antman, *Nonlinear Problems of Elasticity*, (Springer, New York, 2004).
[2] M. Gazzola, L. Dudte, A. McCormick and L. Mahadevan, *R. Soc. Open Sci.* **5**, 171628 (2018).
[3] M. Bergou, M. Wardetzky, S. Robinson, B. Audoly, and E. Grinspun, *ACM TOG* **27** (3), 63:1 (2008).
[4] A. E. H. Love, *A treatise on the mathematical theory of elasticity*, (Cambridge University Press, Cambridge, 1892).
[5] A. Majumdar and A. Raisch, *Nonlinearity* **27** 2841 (2014)
[6] O. Rodrigues, *Journal de Mathématiques* **5**, 380 (1840).
[7] C. Haines, N. Li, G. Spinks, A. Aliev, J. Di, and R. Baughman, *Proc. Natl. Acad. Sci. USA* **113** (42), 11709 (2016).
[8] L. R. G. Treloar, *Trans. Faraday Soc.* **40**, 59 (1944)
[9] S. Reese, P. Wriggers, *Comput. Methods Appl. Mech. Eng.*, **148** (3-4), 279 (1997).
[10] O. Ahumada, M. Cocca, G. Gentile, E. Martuscelli and L. D'Orazio, *Textile Research Journ.* **74** (11), 1001 (2004).

[11] D. Clark, *et al.*, *Phys. Med. Biol.* **41** (7), 1233 (1996).
[12] K. Klenin and J. Langowski, *Biopolymers* **54** (5), 307 (2000).
[13] A. Ghatak and L. Mahadevan, *Phys. Rev. Let.* **65** 057801 (2005).
[14] J. W. S. Hearle and A. E. Yegin, *Journal of The Textile Institute* **63** (9), 490 (1972).
[15] M. Ganji, *et al.*, *Science* **360**, 102 (2018).
[16] B. Soh, *et al.*, *Soft Matter* **14** (9), 1689 (2018).
[17] G. Fudenberg, M. Imakaev, C. Lu, A. Goloborodko, N. Abdennur, L. Mirny, *Cell Reports* **15**, 2038-49 (2016).
[18] J. Yuan, *et al.*, *Science* **365**, 155-158 (2019).
[19] Note that the authors of [10] found nylon's Young's modulus to be approximately 10 times larger than the $E = 30$ GPa modulus we use. However, [11] and Poly-Tech Industrial both describe nylon 6/6 as having a Young's modulus comparable to the one we use. We found that the exact Young's modulus has little bearing on the results of the nylon simulations performed here.
[20] To sum up the notation: a_0 is the initial filament rest configuration radius, a is the filament rest configuration radius at any time during the simulation (hence a can change as a function of time as we actuate the coil), and $\tilde{a}$ is the deformed filament radius at any time (hence $\tilde{a}$ can also change over time and is equal to a in the absence of strain)
[21] We wanted to damp translational but not angular motion in this simulation, since we are concerned with the rate of filament untwist. Hence, we introduce two separate damping parameters, γ_{trans} and γ_{ang}, to damp translational and angular motion, respectively. Here, $\gamma_{\text{ang}} = 12.5$ kg/ms $\approx 2.7\gamma_{\text{char}}$ and $\gamma_{\text{trans}} = 500$ kg/ms $\approx 109.3\gamma_{\text{char}}$.